Frequency comb Brillouin microscopy

Submitted in fulfillment of the requirements for the degree of

Doctor of Philosophy

by

FELIPE ADEMIR ALEMAN HERNANDEZ

UNIVERSITY OF GOTHENBURG

Göteborg, Sweden 2021

Doctoral Dissertation in Physics

Department of Physics
University of Gothenburg
412 96 Gothenburg, Sweden

October 11, 2021

ISBN: 978-91-8009-538-9 (PRINT)
ISBN: 978-91-8009-539-6 (PDF)
URL: http://hdl.handle.net/2077/69706

Cover: Optical layout of a frequency comb Brillouin microscope. Zoomed inset is the 3D plotted BLS intensity vs the spatial coordinates of ultrafast excited phonons on a metallized sapphire crystal.)

Printed by Stema AB, Borås, 2021

Typeset using LaTeX

SVANENMÄRKET
Trycksak
3041 0234

ABSTRACT

Brillouin light scattering (BLS), an almost a century old technique, has evolved into a powerful and versatile method to study acoustic and magnetic phenomena down to the nanometer size scale. Presently, BLS can be applied in fields as diverse as acoustics, spintronics, geosciences and biophysics. In addition, the advent of ultrafast laser sources has seeded interests in studies of light-matter interactions under extreme conditions. Despite the capabilities and unique information that BLS can provide, it suffers from highly demanding and complex instrumentation. Brillouin spectrometers tend to be large, expensive and highly sensitive devices. This has delayed the progress of ultrafast applications of BLS compared to other successful coherent spectroscopic techniques.

This thesis aims to contribute to this nascent field by introducing a new concept named frequency comb Brillouin microscopy. This method exploits the highly structured properties of a GHz repetition rate frequency comb as a pump to selectively enhance the Brillouin scattering intensity, while retaining the inherent high spectral resolution of BLS. Furthermore, due to the impulsive character of the frequency comb, ultrafast generated quasi-particles can be observed. Applications of this technique include the direct observation in frequency domain of ultrafast demagnetization dynamics, ultrafast formation of phononic combs, Brillouin imaging of phonon and spinwave caustics, excitation of quantized perpendicular spinwave modes and selective scattering enhancement of Brillouin modes, to mention a few presented in this thesis.

In a pursuit to overcome the instrumental complexity of BLS spectrometers, and to develop a merchantable instrument which can be used for spintronics research, this thesis also explores alternative Brillouin instrumentation methods. For this purpose, first a virtual-image phase array spectrometer was evaluated for studies of thin magnetic films. Secondly, an apparatus based on the magneto-optical Kerr effect and very high speed electronics was devised and tested in spintronic devices. Implementations here include contact-less ferromagnetic resonance (FMR) spectroscopy of spin-Hall nano-oscillators (SHNOs), phase-resolved imaging and fast acquisition of synchronization maps in SHNO networks for future oscillator-based computing schemes.

Keywords: *Brillouin light scattering*, *Fabry-Perot interferometer*, *spinwave*, *acoustic phonon*, *virtual-image phase-array*, *frequency comb*, *Frequency-resolved magneto-optical Kerr effect*, *spin-Hall nano-oscillator*, *ferromagnetic resonance*, *microscopy*.

ACKNOWLEDGEMENT

The work described in this thesis and the attached papers were only possible through collaborative effort. I could not be successful in this project without the combined effort, in-depth discussions, motivation, and constructive criticism of my colleagues. I want to thank all the co-authors of the papers attached to this thesis for making its publication possible; Jan-Åke and Mats for their practical support; my examiner Johan Åkerman, to provide the means, guidance and support to make this project possible; my supervisor Dag Hanstorp, for his constant help, advice and enthusiasm throughout this journey; to my co-workers Ahmad and Shreyas, with whom I shared deep discussions and many hours of work in the laboratory; to all the administration staff of the University of Gothenburg, to make my academic life easier; I would like to extend my thanks to all the students and members of our group with whom I shared many experiences, discussions and good times; a special thanks to Richard and Remi for their valuable corrections and comments on my thesis. Of course, this research would not be possible without the Swedish taxpayers and the Swedish Research Council. Finally, I couldn't get this far without my life partner, Adriana, to whom I dedicate this success.

Place: Göteborg

Date: 10/10/2021 **Felipe Ademir**

List of publications included in this thesis

I **"Frequency comb enhanced Brillouin microscopy"**

Ademir Alemán[1], Shreyas Muralidhar[1], Ahmad A. Awad[1], Johan Åkerman[1], and Dag Hanstorp[1]

[1]University of Gothenburg, Sweden

Published by: Optics Express Vol. 28, Issue 20, pp. 29540-29552 (2020).
DOI: https://doi.org/10.1364/OE.398619

Contribution: Conception, design and construction of the instrument. Development of control software. Calibration and characterization. Measurement and data analysis. Theoretical description. Main writer of the manuscript.

II **"Sustained coherent spin wave emission using frequency combs"**

S. Muralidhar[1], A. A. Awad[1], A. Alemán[1], R. Khymyn[1], M. Dvornik[1], D. Hanstorp[1], and J. Åkerman[1]

[1]University of Gothenburg, Sweden

Published by: Phys. Rev. B 101, 224423 – 15 June 2020.
DOI: https://doi.org/10.1103/PhysRevB.101.224423

Contribution: First shared authorship. Construction of the setup. Experimental design. Measurement and data analysis. Physical interpretation. Assistance in writing the manuscript.

III **"Femtosecond Laser Pulse Driven Caustic Spin Wave Beams"**

Published by: S. Muralidhar[1], R. Khymyn[1], A. A. Awad[1], A. Alemán[1], D. Hanstorp[1], and J. Åkerman[1]

[1]University of Gothenburg, Sweden

Published by: Phys. Rev. Lett. 126, 037204 – 22 January 2021.
DOI: https://doi.org/10.1103/PhysRevLett.126.037204

Contribution: Construction of the setup. Experimental design. Measurements. Assistance in writing the manuscript.

IV **"Thickness dependent efficiency of femtosecond laser comb driven spinwave excitation"**

A. A. Awad [1], S. Muralidhar [1], A. Alemán [1], R. Cichelero [1], R. Khymyn [1], A. Dmitriev [1], D. Hanstorp[1] and J. Åkerman[1]

[1]University of Gothenburg, Sweden

Manuscript in preparation

Contribution: Construction of the setup. Experimental design.

V **"Real-space imaging of laser-driven phononic combs"**

A. Alemán[1], S. Muralidhar[1], A. A. Isacsson[2], R. Khymyn[1], A. Awad[1], J. Åkerman[1] and D. Hanstorp[1]

[1]University of Gothenburg, Sweden [2]Chalmers university of technology, Sweden

Manuscript in preparation

Contribution: Construction of the setup. Experimental design. Measurement and data analysis. Theoretical description. Main writer of the manuscript.

VI **"An FR-MOKE read-out platform for spin Hall nano-oscillators devices"**

A. Alemán[1], S. Muralidhar[1], A. Houshang[1], A. A. Awad[1], J. Åkerman[1] and D. Hanstorp[1]

[1]University of Gothenburg, Sweden

Manuscript in preparation

Contribution: Conception, design and construction of the instrument. Experimental design. Development of control software. Calibration and characterization. Measurement and data analysis. Main writer of the manuscript.

List of publications not included in this thesis

I **"Photoelectron angular distributions in photodetachment from P^-"**

O. Windelius[1,2], J. Welander[1], A. Alemán[1], D. J. Pegg[3], K. V. Jayaprasad[4], S. Ali[5], and D. Hanstorp[1]

[1]University of Gothenburg, Sweden [2]Chalmers University of Technology, Sweden [3]University of Tennessee, USA [4]Cochin University of Science and Technology, India [5]University of Gujrat, Pakistan

Published by: Phys. Rev. A 103, 033108, 15 March 2021
DOI: https://doi.org/10.1103/PhysRevA.103.033108

II **"Tracking the collision, coalescence and mixing of airborne droplets using optical tweezers"**

S. Radhakrishnan[1], D. Hanstorp[1] and A. Alemán[1],

[1]University of Gothenburg, Sweden

Manuscript in preparation

III **"Optothermal control of spin Hall nano-oscillators"**

S. Muralidhar[1], A. Houshang[1], M. Zahedinejad[1], A. Alemán[1], A. A. Awad[1], R. Khymyn[1], M. Dvornik[1], and J Åkerman[1],

[1]University of Gothenburg, Sweden

Manuscript in preparation

IV **"Observation of FRET in collision of droplets"**

S. Radhakrishnan[1], A. Alemán[1], P. T. Bhaskaran[2], D. Hanstorp[1]

[1]University of Gothenburg, Sweden [2]Cochin University of Science and Technology, India

Published by: Proceedings Volume 11083, Optical Trapping and Optical Micromanipulation XVI; 110832U, 2019.
DOI: https://doi.org/10.1117/12.2528390

V **"A versatile system for optical manipulation experiments "**

D. Hanstorp[1], M. Ivanov[2], A. Alemán[1], J. Enger[1], A. M. Gallego[3], O. Isaksson[1], C. Karlsson[1], R. M. Villa[3], A. Varghese[4], K. Chang[1]

[1]University of Gothenburg, Sweden [2]Vilnius University, Lithuania [3]Universidad Nacional Autonoma de Mexico, Mexico [4]Cochin University of Science and Technology, India

Published by: Proceedings Volume 10347, Optical Trapping and Optical Micromanipulation XIV; 103472C, 2017
DOI: https://doi.org/10.1117/12.2272983

VI **"Optimizing Ti:Sapphire laser for quantitative biomedical imaging"**

J. James[1], H. Thomsen[1], D. Hanstorp[1], A. Alemán[1], S. Rothe[2], J. Enger[1], M. B. Ericson[1]

[1]University of Gothenburg, Sweden [2]CERN, Switzerland

Published by: Proceedings Volume 10498, Multiphoton Microscopy in the Biomedical Sciences XVIII; 1049824, 2018
DOI: https://doi.org/10.1117/12.2286732

TABLE OF CONTENTS

Preface

The present work summarizes results from a collaborative project between the spintronics division and the atomic physics division at the University of Gothenburg (GU). My specialization is in laser physics, optics and optical spectroscopy. During my PhD I extended my collaboration to several other projects, bringing my knowledge in optical instrumentation to the fields of optical and acoustic levitation, negative ion spectroscopy, development of general purpose laser systems and an industry internship with NanoOsc AB. However, I decided to limit this thesis only to my main research project where I contributed by combining optics and spintronics.

This thesis aims to give an overview of my research into developing optical techniques and instruments which are currently used at the forefront of spintronics research at GU. In Chapter 1, a brief historical introduction to spectrocopy and the role of light in magnetism and acoustics is given. Chapter 2 condenses the background theory behind Brillouin light scattering; it contains a glance to the different instrumentation approaches used in this work, followed by a review on ultrafast excitation and coherent control. Finally, a review of the principles which lead us to the main technique developed in this work, which I call *Frequency comb Brillouin light scattering microscopy* (FC-BLS) is presented. The development of an instrument utilizing this technique, and my work developing two alternative Brillouin spectroscopic approaches are presented in Chapter 3. Chapter 4 presents a summary description of the experimental results presented in the appended papers and the results obtained from the Brillouin instruments I built during my PhD. Finally, Chapter 5 closes by summarizing the outcomes of this thesis and my conclusions on the scope of the techniques I have developed.

CHAPTER 1

Introduction

The term optical spectroscopy refers commonly to the wavelength-dependent response of light interacting with matter. The spectra resulting from these interactions yields physical information about the sample of interest under certain environmental conditions. The term spectrum was introduced by Issac Newton in the mid 1600s to describe the dispersion of sunlight by a prism. Newton performed the very first spectroscopic analysis by decomposing the sunlight into its components and concluded that white light consists of a combination of the rainbow colors [1].

More than one century after Newton's first spectroscopic research a series of experiments on the footprint emission and absorption of electromagnetic radiation in gases and the careful analysis of the solar spectrum founded the basis of modern spectroscopy. During the early 1800s, William Herschel and W. Ritter further developed Newton's prism experiment and discovered the infrared and ultraviolet radiation which lie outside the visible spectrum. Concurrently, H. Wallaston enhanced the dispersive power in Newton's experiment by introducing a narrow slit and discovered dark fringes in the solar spectrum. Some years later Fraunhofer independently observed and cataloged the fringes in the spectrum of the sun and other celestial bodies, which he found appear differently. Fraunhofer concluded that the fringes originate somehow at the celestial bodies themselves[2].

Moving forward in the timeline, in the mid 1800s several scientist, such as L. Foucault and J. Ångström, observed and studied the emission and absorption of light by gases, which occur at very specific wavelengths characteristic to each compound. Later, in the 1860s, scientists G. Kirchhoff and R. Bunsen performed a detailed study based

on the ideas and methods provided by their predecessors and determined that the dark fringes in the solar spectrum studied by Fraunhofer correspond to the absorption lines of the different chemical compounds. In this way, Bunsen and Kirchhoff established the methods of modern spectroscopy by demonstrating a link between a chemical's composition and its unique spectral footprint [3].

Today, with the advent of advanced light sources, instruments and new discoveries on the interaction of light with matter, a myriad of spectroscopic techniques have been developed, and constitute the basic analytical tool in any modern laboratory, industry or university [4]. To mention just a few examples, optical spectroscopy can give information on a sample's constituents, such as crystallographic arrangement [5–8], electronic bonds and vibrational states [9–11] from the macroscopic scale to a single molecule [12–14]. It can provide information of time-dependent dynamics such as chemical reactions [15–17] or electronic state evolution down to the attosecond time scale [18–20].

Among the diverse spectroscopic methods, this work focuses on Brillouin light scattering (BLS). This particular method dates from almost a century ago and was first exploited to perform analysis of low frequency mechanical vibrations (acoustic phonons) [21–24]. It was soon realized that BLS could be used to also study excitations of magnetic origin (spinwaves). In the past two decades, BLS has consolidated into a top technique for studies of complex magnetic phenomena by allowing scientists to access information hardly accessible by non-optical techniques [25–30].

The link between optics and magnetism was discovered around the mid 1800 and is historically attributed to Michael Faraday, who performed the first systematic studies on the direct influence on light by a magnetic field [31]. Nowadays this effect is known as Faraday rotation manifests as a rotation of the polarization of a light beam as it propagates through a magnetized medium. The relationship between magnetism and light was formalized when C. Maxwell published his "Dynamical Theory of the Electromagnetic Field" in 1865 [32]. Later, in 1877, John Kerr discovered that not only the state of polarization changes as it traverse an magnetized medium, but also when it is reflected by a boundary of the medium. [33]. This later phenomenon known today

as magneto-optical Kerr effect (MOKE) leads to the change of the polarization state of the light after being reflected by a magnetized surface.

As investigations in this field continued and new light sources became available, new magneto-optical effects were discovered, such as inelastic light scattering from magnetized materials, magnetic circular dicrhoism or magnetic second harmonic generation, to mention some examples [34]. By the end of the 1800s it was clear that light can be affected by a magnetic field, but, it was unclear if the opposite was true, *i.e* that light can produce a change in the magnetization of a medium. This question was solved almost a century later when the inverse counterpart of the Faraday effect was demonstrated both theoretically and experimentally [35].

Today, the experimental demonstration of several magneto-optical effects has revealed that a light field can effectively drive magnetization dynamics. Perhaps the most astonishing discovery in this field was made in 1996 when Beaurepaire *et al.* [36] showed that a femtosecond laser pulse is able to induce ultrafast demagnetization and spin dynamics in Nickel on the previously unimaginable picosecond timescale. This opened the door to intensive studies to understand the spin dynamics at the sub-picosecond time scale. Immediately after this discovery, the prospective technological applications on optical magnetic writing and magnetic-based data processing at faster rates became evident [37–40].

Since the pioneering work of Beaurepaire's group, it has been proven by many other groups that a single femtosecond laser pulse action can trigger an ultrafast magnetic response in a variety of forms such as ultrafast demagnetization [41–44], optically coherent generation of spinwaves [45–47], all optical magnetic switching [48, 49] and laser induced modification of the magnetic structure [50]. The origin of these ultrafast phenomena is still under debate and several mechanisms have been proposed by the scientific community [51]. The problem is extremely complex since the phenomena appear in different forms being strongly dependent on the optical, thermal and magnetic characteristics of the material.

With the development of commercial mode-locking lasers, the field of picosecond

and subpicosecond laser ultrasonics developed in parallel with the field of ultrafast magnetism [52–55]. In the acoustic case, the laser pulse transfers energy into the lattice, launching a coherent phonon wave. The mechanisms of the generation of coherent acoustic phonons (CAP) by laser action are more established than the magnetic counterpart although debate in the scientific community is still going on [56].

In general, the mechanism of generating CAP depends on the sample's properties (optical, thermal, mechanical, crystal structure, etc) and the laser characteristics. It can be thermal [57–59], photoinduced (by hot electrons generated via optical transitions) [60, 61] or in some materials purely optical (electrostriction) [62, 63]. This last mechanism correspond to a stimulated Raman transition by the laser and has been observed experimentally mostly in transparent materials where other thermal effects are small.

Coherent control of phonon modes has been accomplished experimentally by the use of double-pulse excitation. Multi-pulse methods have been proposed for the optical generation of frequency-tunable acoustic phonons [64–66]. In such experiments a finite optical pulse train with a variable repetition rate ranging from some GHz to THz was produced to selective excite the phononic system. Continuous pulsed pumping by a high repetition rate laser source has been reported recently [67–69]. In this type of experiments the exited acoustic mode has a higher frequency than the repetition rate used for pumping and the excitation occurs when the pumping frequency matches a subharmonic of the acoustic mode.

Ultimately, ultrafast optical manipulation is not limited to the control of mechanical and magnetic states. A dream is the ability to fully control all matter properties by light and the direct visualization of its dynamics. This thesis aims to scientifically contribute to this objective by developing an instrument based on BLS combined with a GHz frequency comb laser source (an infinite pulse train). This method provides a mechanism to selectively excite high-amplitude coherent magnon and phonon modes while simultaneously allowing characterization in the frequency domain using BLS detection.

CHAPTER 2

Theory and analytical techniques

2.1 Light scattering

The term light scattering applies to physical phenomena whereby electromagnetic radiation changes its trajectory due to its interaction with the medium in which it is propagating. Forms of scattering include the common phenomena of reflection and refraction of light and the diffusive scattering by a turbid medium. Such forms of scattering do not change the energy of the scattered wave and are called elastic scattering. A very important form of elastic scattering named after physicist Lord Rayleigh occurs when light interacts with particles much smaller than the wavelength of the incident radiation. So-called Rayleigh scattering occurs when the electric field of the light causes the particle charge to oscillate with the same frequency as the light field and therefore the particle becomes a radiating dipole. Rayleigh scattering may occur in any forms of matter due to the interaction of light with the atoms or molecules of the medium.

The second type of scattering which involves a change in the energy of the scattered wave is called inelastic scattering. Here, the incident electromagnetic field exchanges energy with the medium. If the field gains energy (blue shifted) the process is referred to as an anti-Stokes process and if it loses energy (red shifted) as a Stokes process. In the medium, this exchange of energy is manifested as the annihilation or creation of collective excitations or quasi-particles such as phonons and magnons. Figure 2.1 exemplifies the energy diagrams of these processes for an incident photon with energy $\hbar\omega$ and an excited state with energy $\hbar\omega$, where $\hbar$ is the reduced Planck constant, ω angular frequency of the light, and Ω the angular resonance frequency of the state.

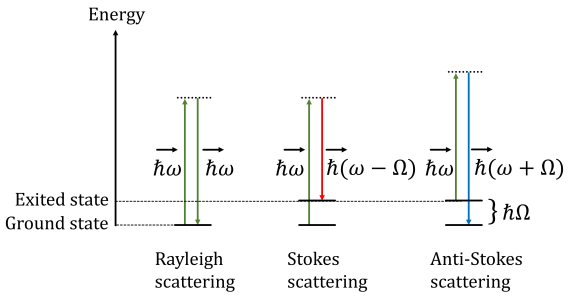

Fig. 2.1 Different possibilities of light scattering by a medium.

The action of the light electric field is to drive the charged particles of the medium. At visible spectral frequencies atoms are too heavy to adiabatically follow the fast oscillations of the light field. Electrons, however, are light enough to follow the oscillations of the driving electric field. As a result of the displacement of negative charges from their equilibrium position, a dipole moment is induced in the medium. In the absence of inelastic processes and for weak electric fields the polarizability of the medium is described by the macroscopic polarization density

$$P(t) = \epsilon E(t). \tag{2.1}$$

Here ϵ is the dielectric permitivity constant of the material, which is in general a tensor quantity. Hence the dipole moment induced by the electric field is responsible for the re-radiation of the energy at the same frequency as $E(t)$.

2.2 Microscopic origin of scattering

It is common knowledge that light traveling from vacuum to an optically transparent material will refract and slow down when entering into the material. It is also well known that light traveling in vacuum has an universal constant velocity c and that the observed velocity of the light after entering the glass is c/n, where n is the index of refraction of the material. On an atomic scale, light entering a medium will oscillate resonantly with the bound electrons of the medium. These electrons vibrate at the same

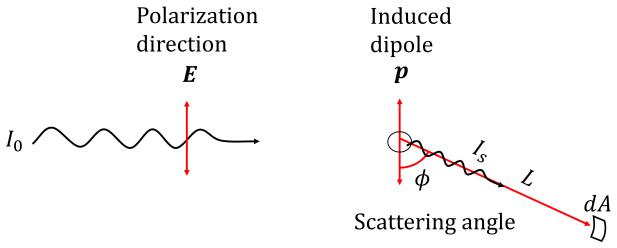

Fig. 2.2 Geometry of light scattering from a single scatterer.

frequency as the incident light and become radiating sources. The strength of this disturbance in the electronic system is dependent on the electric susceptibility of the medium χ_e. Due to the superposition principle in Maxwell's equations, the observed field propagating in the material will be a sum of the contributions from the incoming field and the field produced by the oscillating electrons of the medium. As a matter of fact, each independent field created by each electron travels at the speed of light in vacuum c, but when all propagating waves are added coherently the resultant macroscopic wave is observed to travel with a reduced speed by a factor $1/n$ in the forward direction.

Let us consider an incident polarized light beam in a material where N atoms or molecules are illuminated. Assume the wavelength λ of the light is much larger than the dimensions of a single molecule of the system, which is the case for visible light, UV and IR radiation. In response to the electric field of the light each molecule in the medium will develop a dipole moment

$$p = \epsilon_0 \alpha(\omega) E_0 \exp(-i\omega t). \tag{2.2}$$

where $\alpha(\omega)$ is the polarizability of each particle, $\omega = 2\pi/\lambda$, ϵ_0 is the vacuum permittivity, and where $E_0 \exp(-i\omega t)$ is the same incident field for each particle. It is then shown in [70] that the intensity of the scattered light from the induced radiating dipole from Eq. 2.2 at a distance L is given by

$$I_0 = \frac{n\omega^4 \epsilon_0 |\alpha(\omega)|^2 |E_0|^2}{8\pi c^3 L^2} \sin^2 \phi. \tag{2.3}$$

Here the angle ϕ is defined by the dipole vector and the vector to the point of observation, as shown in Fig. 2.2. The differential cross section of scattered light falling into a detector of area dA is defined as

$$\frac{d\sigma}{d\Omega} = \frac{I_s}{I_0}\frac{dA}{d\Omega} = \frac{I_s}{I_0}L^2. \tag{2.4}$$

Without explicitly writing $\alpha(\omega)$, Eq. 2.3 and 2.4 predict two important results from scattering theory:

1- The scattering intensity I_s is proportional to the fourth power of the frequency of the incident radiation.

2- There is no scattering in the direction of the polarization of the incident light.

2.3 Quantum perspective of inelastic light scattering

The general mechanism of scattering is due to the motion of charged particles in the medium driven by the electric field of the light. However, since the electrons are bound to the nuclei, their motion is also affected by the nuclear mobility. Hence, the dipole moment of the electrons is modulated in the presence of nuclear vibrational modes because the nuclear potential that the electron experiences depends on the atomic coordinates.

From a classical view, the scattering process by an elementary excitation can be understood as a result of a modulation of the dielectric permitivity tensor ϵ_{ik} by the quasi-particle oscillation. In the first order perturbation expansion of the polarization density vector $\delta\boldsymbol{P}(\boldsymbol{r},t)$ induced by the incoming field $\boldsymbol{E}^I$ is given by

$$\delta\boldsymbol{P}_i(\boldsymbol{r},t) = \delta\epsilon_{ij}(\boldsymbol{r},t)\boldsymbol{E}^I_j. \tag{2.5}$$

Here, in contrast to the elastic case, the induced dipole serves as a radiating source at a frequency given by the product of the modulation wave $\delta\epsilon_{ij}$ and the incoming field. In a quantum mechanics picture (see diagramn in Fig. 2.3) this corresponds to a three particle process in which a photon with frequency and wavevector $(\omega_i, \boldsymbol{k}_i)$ exchanges energy with the medium resulting in the creation/annihilation of an elementary excitation with

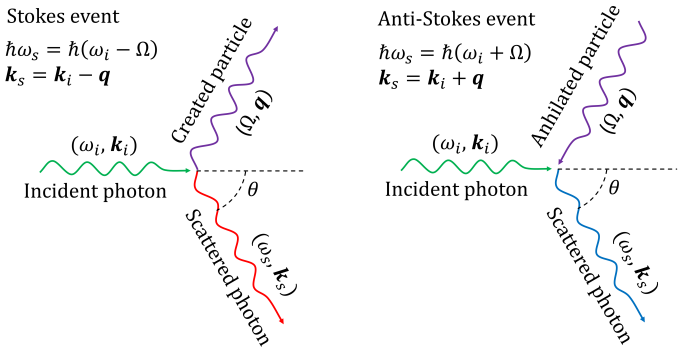

Fig. 2.3 Kinematics of the BLS process

frequency and wavevector $(\Omega, \boldsymbol{q})$ and the re-emission of the photon as a scattered wave with frequency and wavenvector $(\omega_s, \boldsymbol{k}_s)$. Energy and momentum should be preserved, which requires that

$$\begin{aligned} \boldsymbol{k}_s - \boldsymbol{k}_i &= \pm \boldsymbol{q} \\ \omega_s - \omega_i &= \pm \Omega, \end{aligned} \tag{2.6}$$

in which the plus sign refers to an anti-Stokes event where a quasi-particle is annihilated and the scattered photon shifts to the blue side of the spectrum and the minus sign corresponds to a Stokes event where an excitation is created and the scattered photon looses energy shifting to the red side of the spectrum.

The quantities Ω and $\boldsymbol{q}$ are related to the scattering kinematics trough the set of equations

$$\begin{aligned} |\boldsymbol{q}| &= 2n|\boldsymbol{k}_i|\sin\frac{\theta}{2} \\ \Omega &= 2nv|\boldsymbol{k}_i|\sin\frac{\theta}{2} \\ v &= \frac{\Omega}{|\boldsymbol{q}|}, \end{aligned} \tag{2.7}$$

where n is the refraction index of the material, θ is the scattering angle and v is the

propagation velocity of the quasi-particle.

2.4 Brillouin light scattering from acoustic phonons and spinwaves

Brillouin light scattering (BLS) is a form of inelastic scattering in which light interacts with large scale excitations in a medium. In contrast to Raman scattering, which is due to single molecular bonds of neighbor atoms, Brillouin scattering takes place due to the extended collective oscillations in a medium, such as acoustic phonons or spinwaves. Even though BLS is a microscopic phenomenon and should be described by the formalism of quantum mechanics, an heuristic classical treatment can be employed to describe the scattering as a consequence of the modulation of the dielectric susceptibility of a medium by thermal fluctuations.

The instantaneous dielectric susceptibility tensor in the presence of thermal phonons can be described by

$$\chi_{ij} = \chi\delta_{ij} + \delta\chi_{ij}, \tag{2.8}$$

where χ is the dielectric susceptibility constant for an isotropic material and $\delta\chi_{ij}$ is the modulated fluctuation due to thermal phonons. The corresponding time-dependent component of the dielectric permitivity is then given by

$$\delta\epsilon = \epsilon_0\delta\chi_{ij}. \tag{2.9}$$

Thus, the modulation component of the polarization density vector can be written as $\delta\boldsymbol{P}_i = \delta\epsilon_{ij}\boldsymbol{E}_j$. The total field $\boldsymbol{E}_j$ is given by the sum of the incident and the scattered field

$$\boldsymbol{E}_j = \boldsymbol{E}_j^I + \boldsymbol{E}_j^S. \tag{2.10}$$

As both, the scattered field $\boldsymbol{E}_j^S$ and $\delta\epsilon_{ij}$ are small quantities, the time-dependent polarization density can be approximated by Eq. 2.5. Here, the radiating source of scattering waves $\delta\boldsymbol{P}_i$ is driven uniquely by the incident electric field.

Light scattering from spinwaves might be expected to occur due to a direct interac-

tion of the spin lattice and the magnetic vector of the light field. However, this mechanism has been shown to be extremely weak and the dominant modulation of the dielectric permitivity due to spinwaves is instead mediated via spin-orbit coupling. Thus, scattering from spinwaves can be described with the same treatment as for phonons. For ferromagnets, the magnetic modulation of the permitivity tensor, $\delta\epsilon_{ij}$, can be represented in terms of a power expansion of the magnetization vector M [71],

$$\delta\epsilon_{ij} = f_{ik\alpha}M_\alpha + g_{ik\alpha\beta}M_\alpha M_\beta, \tag{2.11}$$

where f and g are complex tensors. For antiferromagnets, Eq. 2.11 holds with the substitution of M by the antiferromagnetic vector $L = M_1 - M_2$, where M_1 and M_2 are the sublattice magnetizations. Thus, the time-dependent modulation of M caused by thermal spinwaves provides a mechanism for Brillouin scattering under the same arguments used for the description of scattering by phonons.

Brillouin scattering polarization selection rules allow us to recognize the nature of the scattering. Due to the nature of the Lorentz force, the modulation of the polarization vector of a medium by spinwaves is transversal to the incident electric field. In general, the polarization of the scattered field from magnetic excitations is rotated with respect to the incident field polarization. In particular, in a back-scattering geometry, the field scattered by magnons is linearly polarized and rotated by 90° [71]. In the case of phonons, the polarization of the scattered field can be either in the same axis of the incident field polarization for longitudinal modes or depolarized with no component along the scattering plane for transverse modes. As a consequence, and due to momentum conservation, the scattering amplitude of transversal phonons falls to zero in a back-scattering geometry [21]. These selection rules are particularly advantageous in this work where a reflective microscope geometry is implemented.

2.5 Stimulated Brillouin scattering

Scattering is stimulated if it is induced by the presence of a second light field which drives the material into resonance. The conditions for stimulated Brillouin scattering (SBS) to occur are given by the spectral characteristics of the interacting fields and its strength. If the second light field, called the Stokes field E_s, interferes at the Stokes Brillouin shift $\omega_s = \omega_{pr} - \Omega$, where ω_{pr} is the frequency of the probe field E_{pr} and Ω the excitation frequency, the material tends to increase the amplitude of the scattering due to a resonance effect. The stokes field can be produced by the beating of a second laser source with frequency ω_p, called the pump field E_p, or by the Brillouin field itself. In both cases the intensity of the beams should be large enough to induce a non-linear polarization in the material. Such non-linearities are included in the macroscopic polarization density expanded in higher power terms of the field

$$P(t) = \epsilon_0[\xi^{(1)}E(t) + \xi^{(2)}E(t)^2 + \xi^{(3)}E(t)^3 + ...]. \tag{2.12}$$

Here $\xi^{(n)}$ is the n^{th}-order susceptibility. Due to symmetry constraints, the second-order susceptibility vanishes for most materials with the exception of noncentrosymmetric crystals. Stimulated scattering is ruled by the third-order susceptibility and the triple product $E_p E_{pr} E_s$ of the interacting fields. Figure 2.4 shows the energy transfer in the Stokes/anti-Stokes SBS process.

Another important characteristics of SBS is that the scattered field is coherent. In spontaneous Brillouin scattering the phase of the Brillouin oscillation is determined by the random phase of the thermal fluctuations of the material. Conversely, in the stimulated case, the phase of the Brillouin oscillation is set by the phase difference of the input probe and stokes fields. Hence, in SBS the sample is set to a coherent state by the interacting fields. The total BLS intensity I_{BLS} is proportional to $\langle \sum_i E_i \rangle$, where E_i is the field contribution from the i^{th} emitter or excitation. For spontaneous scattering the population of emitters are incoherent, *i.e.* $\langle E_i E_j \rangle = 0$, and hence I_{BLS} is proportional to the number of emitters N. In the stimulated case the emitters are coherent and hence

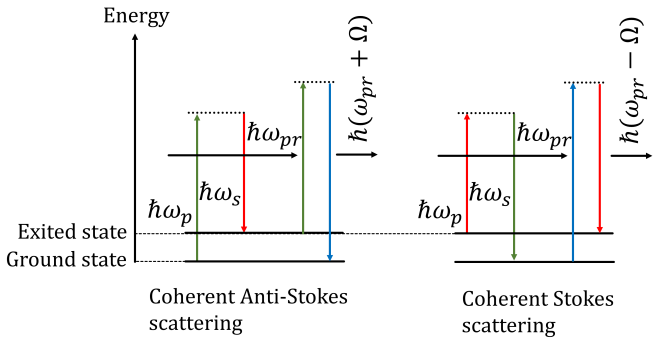

Fig. 2.4 Energy transfer in stimulated scattering. Two photons with energies $\hbar\omega_p$ and $\hbar\omega_s$, known as the pump and Stokes, drive the system coherently. A third photon with energy $\hbar\omega_{pr}$, known as probe, undergoes coherent anti-Stokes scattering annihilating the state. This process is analogous for coherent Stokes scattering which leaves the system in an exited state.

$\langle E_i E_j \rangle = \langle E_i^2 \rangle$, and therefore $I_{BLS} \propto N^2$.

2.6 The Fabry-Perot interferometer

In optical techniques such as Raman scattering or fluorescence spectroscopy, grating spectrometers are sufficient to resolve the typical spectral features. In Brillouin spectroscopy, however, the frequency shift and intensity of the scattered field with respect to the incident field are so small that grating spectrometers with enough resolving power capable to discriminate Brillouin spectral features are economically non-viable and other methods need to be employed.

In Brillouin spectroscopy the standard instrument for analysis is the Fabry-Perot interferometer. A Fabry-Perot interferometer consists of an optical cavity usually constructed by two partially transmitting plane mirrors parallel to each other and separated by a distance L. For a plane-plane optical cavity, the transmission is a periodic function of the wavelength determined by

$$T(\lambda) = \frac{1-R}{1+(4F^2/\pi^2)\sin^2(2\pi L/\lambda),} \tag{2.13}$$

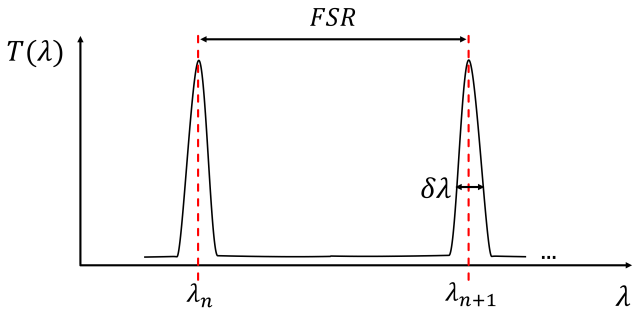

Fig. 2.5 Transmittance of a Fabry-Perot cavity.

where $R < 1$ is a constant which incorporates the losses of the system and F is the finesse of the cavity which represents a quality factor of the construction of the optical cavity.

The period of Eq. 2.13 is know as free spectral range (FSR) and is given by

$$\text{FSR} = \frac{c}{2L}, \tag{2.14}$$

where c is the speed of light.

The transmission bandwidth determines the resolution of the interferometer and is related to the finesse as

$$\delta\lambda = \frac{\text{FSR}}{F}. \tag{2.15}$$

Figure 2.5 shows a plot of the transmittance as a function of wavelength of a Fabry-Perot cavity.

The Fabry-Perot interferometer can be used as a spectrometer by varying the mirror distance L so that the wavelength of the transmitted light is scanned as a function of L. The spectrum under analysis can only be unambiguously discriminated if it lies between the FSR of the cavity. In principle, one can increase the FSR as much as desired. However, due to the constant of Eq. 2.15, the resolution decreases proportional to the increment in the FSR where the finesse F is the limiting factor. The major factors which reduce the finesse of the interferometer are the non-perfect reflectivity of the mirror coatings, the lack of perfect parallelism, flatness of the mirror surfaces and the

spatial uniformity of the light source under analysis. The practical achievable finesse of an optical cavity is < 100 due to mechanical limitations.

From Eq. 2.13 the maximum contrast, *i.e.* the dynamic range of the transmission is determined by the coefficient of the denominator

$$4F^2/\pi^2. \tag{2.16}$$

For a standard Fabry-Perot interferometer the maximum achievable contrast is of the order of 10^3. However, in back-scattering Brillouin microscopy the typical ratios between the fraction of the light which undergoes Brillouin scattering and the residual Rayleigh scattering are in the $10^{10} - 10^{15}$ orders of magnitude. Therefore, the contrast of a single optical cavity is not sufficient to discriminate Brillouin signals from the strong elastic scattering. By passing the light field into N Fabry-Perot cavities arranged in tandem the effective finesse and the theoretical contrast of the tandem Fabry-Perot interferometer scales to the power N. Therefore, by coupling several Fabry-Perot interferometers in tandem one can reach the contrast required for observing weak Brillouin signals. Ultimately, the contrast is limited by cross-talking interference between the cavities, mechanical stability of the alignment and accumulative losses due to imperfection of the mirrors making up to 6-passes in a double pass tandem interferometer the most practical design. Such an instrument was developed by Sandercock and has been the standard in BLS for more than 40 years [72], giving contrast levels up to 10^{15} [73].

2.7 Virtual image phase array spectrometers

A virtual image phase array (VIPA) is a novel type of Fabry-Perot etalon formed by a tiled glass plate with 3 different coatings (see Fig. 2.6). On one side, the plate is coated with a high-reflectivity coating except for a small area at the bottom of the plate which is coated with an anti-reflective layer which serves to couple the light into the etalon. The other face of the plate is coated by a partially reflective coating. When a light beam enters the VIPA, it is reflected several times between the high reflectivity and the par-

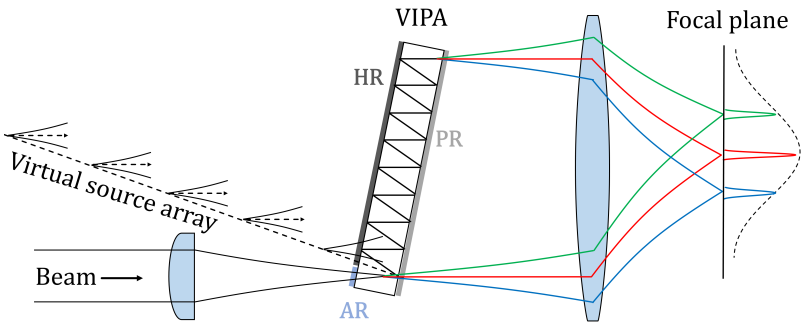

Fig. 2.6 Principle of operation of a VIPA etalon. AR, HR and PR are the anti-reflective, high-reflective and partially-reflective coatings, respectively. Typically, a cylindrical lens is used to focus the beam to line into the AR surface. A virtual image phase array is formed behind the plate which resembles a diffraction grating. A spherical achromat is then used to focus the dispersed beam into a plane. Due to the decaying amplitude of the virtual source array, the intensity at the focal plane follows a lorentzian distribution.

tially reflective surfaces, forming a series of parallel beams emerging from the output coupling surface. These beams appears to come from equally spaced and superimposed virtual sources which form a virtual phase array. Such array can be interpreted as a "grating" formed in a virtual space (in a real grating, a phase array is formed in real space). As in a grating spectrometer, a lens is used to focus the VIPA output to a plane where the light interferes and decomposes into its spectral components. Compared to a grating of the same size, the resolution of a VIPA is 10-20 times higher [74]. This enables a tremendous reduction in the size and the manufacturing cost of high-resolution spectrometers which are based on a VIPA element. A full analytical treatment of the dispersion and transmission function of a VIPA etalon is out of the scope of this thesis and can be found in the work of Hu *et al.* [75].

The tandem Fabry-Perot interferometer (TFPI) developed by Sandercock demands expertise in optics from the operator in order to perform alignment routines, requires active vibration isolation and a large space on an optical table, which increases its price considerably. On the contrary, VIPA spectrometers offer a very affordable and compact design without moving parts, eliminating the need of an isolation base. The recent invention of the VIPA has made Brillouin spectroscopy a more accessible tool for re-

searchers in fields far away from optics such as biophysics and biomedicine [76–78].

2.8 Frequency-Resolved MOKE spectroscopy

Frequency-resolved magneto-optical kerr effect (FR-MOKE) spectroscopy is a very recent developed technique [79] which can be used to retrieve the physical information which is encoded in the Brillouin shift. The correspondence between BLS and FR-MOKE is supported by a recent comparative study performed by Liensberger *et al.* [80] which shows a good agreement between the two techniques. Compared to BLS, where a complex optical analyzer is needed in order to discriminate the spectrum, in FR-MOKE the spectrum is analyzed electrically, and therefore eliminates most of the complexity of the optical instrumentation.

In a FR-MOKE measurement the sample should first be excited to a coherent state through an external radiofrequency (RF) field using a built-in transmission line. At the right excitation frequency the sample experiences a resonance leading to absorption of the RF wave. The sample spectrum can be acquired electronically by measuring the transmitted RF field with a physical probe connection to the sample. FR-MOKE instead exploits the Kerr effect to probe the sample spectrum optically (contact-less) rather than electrically (see Fig. 2.7). Here the sample is probed locally by a focused and linearly polarized laser beam which experiences a Kerr rotation upon reflection off the magnetized surface. The Kerr modulation is proportional to the out-of-plane magnetization m_z and therefore the beam is modulated coherently at the ferromagnetic resonance (FMR) frequency. The modulated optical field is then converted to an electrical signal V_{out} by a high speed photodiode. The signal V_{out} is then compared to the original stimulus signal V_{in} as

$$V_{out/in} = \left|\frac{V_{out}}{V_{in}}\right| e^{i(\theta_{out}-\theta_{in})}, \tag{2.17}$$

where V_{out}/V_{in} indicates the intensity of the detected signal and $\theta_{out} - \theta_{in}$ its phase. The quantity $V_{out/in}$ is also refereed in the literature as the $S_{21}-$parameter or forward

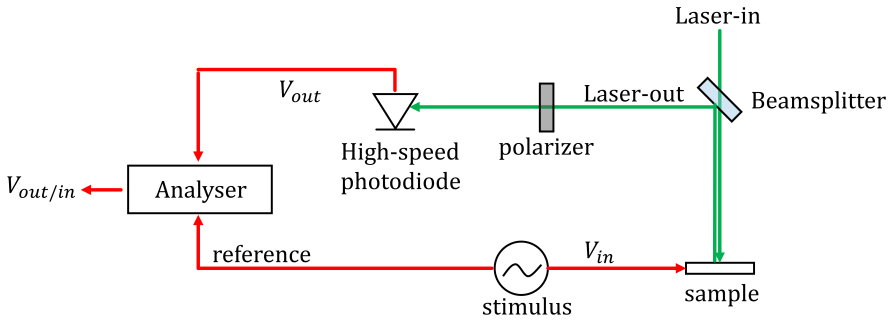

Fig. 2.7 Simplified FR-MOKE setup. The green arrows represent optical paths while the red arrows show physical electrical connections.

scattering parameter.

The main advantage of the FR-MOKE method is that it does not need an optical analyzer to retrieve the magnetization dynamics of the sample, which drastically reduces the complexity of the optical bench used in the TFPI or the VIPA schemes. There are, however, some important differences to notice between FR-MOKE and conventional Brillouin spectroscopy. In BLS the acquired signal is proportional to the intensity of the laser field, and therefore proportional to m_z^2, which means that the phase information is hidden by this relation. In FR-MOKE, on the contrary, the signal is directly proportional to the out-of-plane magnetization ($\propto m_z$). Hence, FR-MOKE gives direct access to the phase information of the magnetization dynamics. As a consequence, BLS can be sensitive to thermal magnetization dynamics, while FR-MOKE can only be use to detect coherent signals stimulated by an external reference source.

2.9 Ultrafast laser excitation of phonons and spinwaves

The creation of quasiparticles like phonons and magnons by ultrashort pulses are physical phenomena with a rich variety of generation mechanisms which are strongly material-dependent. There is not a universal description of the ultrafast phenomena and, furthermore, the underlying physics are not yet well understood by the scientific community. However, most of the common interaction mechanisms of ultrafast action upon a medium can be divided into two categories, named as thermal and optical driven mech-

anisms. In general, several mechanisms from both categories can act together under ultrafast excitation but depending on the sample characteristics one or the other tend dominate.

Thermal effects are mostly dominant in opaque samples and involve the absorption of the laser photons by the electronic system of the material and its subsequent interaction with other degrees of freedom (phononic and spin systems). Optical effects, on the other hand, do not involve the direct absorption of the laser field and are more prominent in transparent materials. Compared to thermal effects, which persist after the pulse has been absorbed, optical effects are mainly based on photon scattering mechanisms and are present only during the laser pulse time duration. There is, however, a myriad of physical phenomena occurring when an ultrashort pulse interacts with specific materials. The field of ultrafast science is extremely vast and an attempt to present a comprehensive insight is out of the scope of this work. For the purposes of this thesis, a description of the more general thermal and optical effects are introduced in the following sections.

2.9.1 Thermal effects

Upon ultrafast laser interaction, the electrons of the medium under irradiation can be heated up on a femtosecond time scale. In metals, laser heating occurs by direct absorption of the photons by the electrons in the conduction band [81]. Additionally, in semiconductors and dielectrics, electron-hole pairs are generated due to the absorption of photons by electrons in the valence band [82, 83]. After the lifetime of the photoexited carriers, the electronic system relaxes and deposits its energy into the lattice leading to an increase in the medium temperature. During this process, the system is under an electronic pressure and lattice heating (also named as phononic pressure) which are responsible of the emission of phonons [56].

The electronic pressure arises because the laser induces a change in the electronic distribution of the material and therefore modifies the overlap integrals of the atoms of the lattice. As a consequence, the equilibrium position of the atoms changes leading to

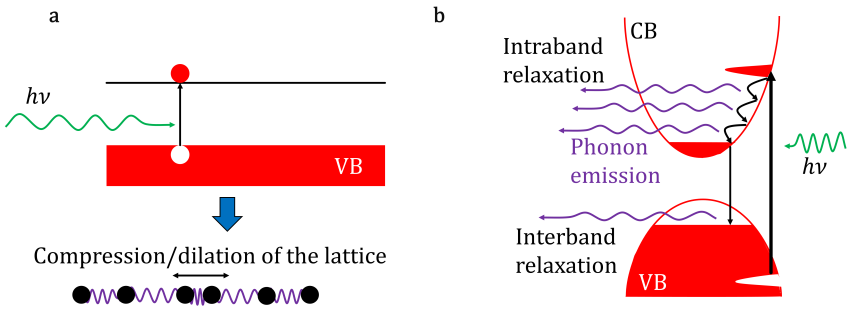

Fig. 2.8 Thermal mechanisms of phonon generation by ultrafast action. CB- conduction band. VB- valence band. Electronic transitions are marked with black arrows. Electronic occupation is shown with red fill. **a.** Electron-hole pairs lead to a change in the electronic distribution. This produces a deformation potential which leads to relocation of the lattice atoms. **b.** In the thermoeleastic effect hot carriers produced by the laser action relax into lower energy states of the CB trough emission of phonons.

expansion and compression, and therefore, to the emission of phonons (see Fig. 2.8a). This mechanism is also termed as the deformation potential [84]. It is mostly relevant in the first picosecond after excitation, after which the electronic system diminishes its temperature by relaxation into the lattice, leading to a longer time scale process called thermoelasticity [85]. This phenomenon is commonly understood as a volume change under a temperature fluctuation and vice-versa. From a quantum perspective the thermoelastic stress is described as an increment in the vibronic energy (increase of phonon population) due to intraband electron-phonon scattering and non-radiative interband recombination (see Fig. 2.8b).

The efficiency of phonon generation by either electronic pressure or thermoelasticity depends on the lifetime of the photoexited carriers. The relaxation of carriers into lower energy states and back to the valence band limits the effectiveness of the deformation potential mechanism to generate phonons. Therefore, this mechanism is most common in semiconductor and dielectric materials with long recombination lifetimes, while for metals the most relevant mechanism for the generation of phonons is thermoelasticity.

In magnetic materials under femtosecond laser action, excited carriers can also relax into the spin reservoir generating spinwaves and ultrafast changes in the magnetization state of the medium. In a typical scenario, the magnetization of the medium is quenched

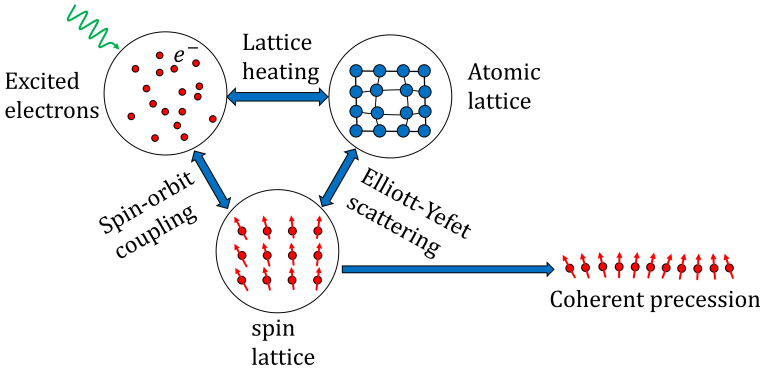

Fig. 2.9 Spin interaction with other degrees of freedom upon laser excitation.

by ultrafast action on a time scale < 1 ps in a process termed ultrafast demagnetization followed by a slow re-magnetization process [86]. During the demagnetization process, spin angular momentum is transferred by spin-flip scattering mechanisms driven by interactions between the electronic, phononic and spin reservoirs (see Fig. 2.9). In materials with strong spin-orbit coupling, electron-electron scattering can contribute to spin momentum transfer since real electronic states do not have a pure spin component but instead a mixed spin state. Separation of the electronic band structure into majority spin-up and minority spin-down states also allows spin flip via the Stoner mechanism [86] whereby an electron undergoes spin reversal by being moved from a majority to a minority band.

Interactions of electrons with the lattice provide a spin-flip mechanism on longer time scales than in electronic interactions [87]. Here, the most accepted theory to the ultrafast demagnetization is the Elliot-Yefet spin-flip process. Elliot-Yefet theory shows that an electron-phonon scattering event changes the spin expectation value of the electron and therefore a spin-flip probability can be assigned [88].

Through the demagnetization process, coherent spinwaves can also be launched into a medium which is exposed to an external magnetic bias [45]. Under ultrafast excitation, the almost instantaneous increase in the electron system temperature causes the system to find a new equilibrium angle in a time scale in between the electron thermalization

time. This is followed by a coherent precession around the external bias field during the remagnetization stage.

2.9.2 Optical effects

In transparent samples, laser fields can induce a notable photostress by polarizing the medium. For the case of phonon generation, this process is called electrostriction. The electrostriction forces exerted by a laser field can distort the atomic orbitals and therefore the electronic distribution leading to a work done by the material [56, 89]. Such distortion occurs when the laser spectrum contains frequency components such that the field is modulated at some phononic resonance of the material.

If the material under excitation is magnetic, spin flip and spinwave generation can be induce by an inverse Faraday effect [90, 91]. In this scenario, a circularly polarized laser field induces a local magnetization proportional to the square of the electric field of the light. The optical generation of acoustic and magnetic perturbations by ultrafast action has a quadratic dependence on the laser electric field and can be viewed in terms of coherent stimulated scattering. Two frequency components, ω_1 and ω_2 contained in the broadband spectrum of the laser field can induce a Brillouin transition Ω mediated by a virtual state. During this process, the orbital momentum of the electrons in the material increases, but if no real electronic transition can occur and the material has a strong spin-orbit coupling, then a spin flip can be induced as well creating or annihilating a magnon [92].

It is important to note that the optical generation of quasiparticles occurs at the fastest possible speed and occur only during the propagation of the laser pulse in the sample. For comparison, Fig. 2.10 shows the typical time-dependent temperature of the electronic, phononic and spin systems in an ultrafast experiment.

2.10 Coherent control using multipulse excitation schemes

Coherent control is the non-contact manipulation of dynamical processes in the quantum world using optical pulses. Optical coherent control has its principle of operation in

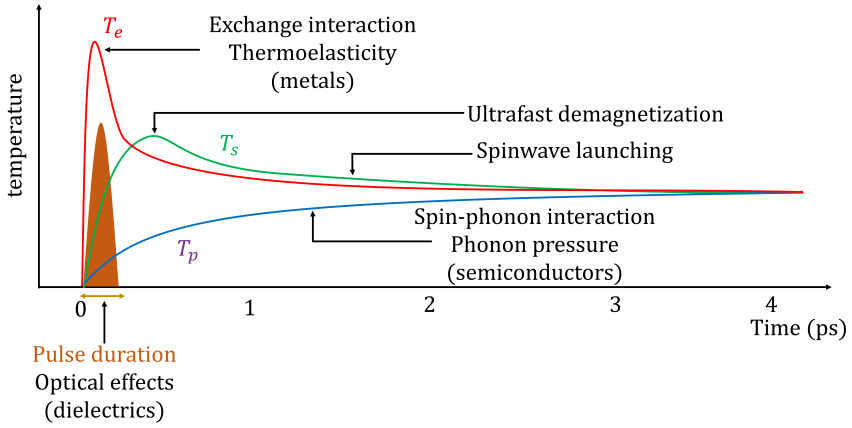

Fig. 2.10 Thermal evolution and typical time scales of ultrafast excitation mechanisms. The pulse duration of typically 30-300 fs is shown in orange. The time dependent temperature of the electronic (T_e), phononic (T_p) and spin systems (T_s) are shown as solid lines is red, blue and green, respectively. The different excitation mechanisms are marked with black arrows at their corresponding time scales in the graph.

the quantum interference of wave functions in matter. In a typical scenario, a quantum system is routed to a broadband coherent excited state by an initial light pulse. Then, a second pulse delayed with respect to the first by a time δt re-excites the system to an additional independent state with a fixed coherence relation to the first excitation. Therefore, the final state will reflect the interference between the two collective wave-functions generated by the two light pulses. By varying the time delay between the two pulses, one can tune this optically induced quantum interference, allowing dynamical control of the system dynamics [93].

Let us consider a vibrational mode with frequency Ω. In SBS, two photons with frequencies ω_1 and ω_2 which fulfill the condition $\omega_2 - \omega_1 = \Omega$ are able to prepare the sample in a coherent state with vibrational energy $\hbar\Omega$. Here, a single ultrashort pulse, where the bandwidth $\delta\omega_p$ exceeds Ω, is capable to induce such coherent oscillation mediated via a virtual state transition. Equivalently, in order to observe a significant excitation by a single pulse, the laser pulse duration $\delta\tau_p \approx 2\pi(0.44\delta\omega_p)$ should be considerably shorter than the excitation period $T_\Omega = 2\pi/\Omega$ [94]. This condition is

known as the impulsive excitation limit. Now, a second pulse arriving at the sample delayed with respect to the first one by δt will pump the system again to the state $\hbar\Omega$ but with a phase difference

$$\delta\phi = 2\pi\frac{\delta t}{T_\Omega} \tag{2.18}$$

with respect to the first excitation.

If we ignore the dephasing and damping of the system it is evident from the phase Eq. 2.18 that a multi-pulse excitation scheme can be used to suppress or amplify the amplitude of the state $\hbar\Omega$ by setting δt equal to $nT_\Omega/2$ or nT_Ω respectively and with n being an integer number. Here, pulses arriving in phase with the excited state period promote only Stokes scattering in the pump pulses, allowing energy to be released into the system. In the same way, pulses arriving out of phase with the excited state will promote anti-Stokes scattering, annihilating the excitation [95].

Let us now discuss in more detail the time-frequency Fourier structure of the excitation by a train of pulses. If low energy states with vibrational frequencies in the GHz range are to be excited, a femtosecond train of N pulses can be well approximated by a Dirac delta comb of the form

$$|E(t)|^2 = \frac{I_0}{N}\sum_{j=1}^{N}\delta(t+(j-1)T_p), \tag{2.19}$$

where T_p is the laser pump train period and I_0 is the pulse train energy. The power spectrum of such a delta train is given by [96]

$$I(\omega_p) = I_0\exp(-i(N-1)\omega_p T_p/2)\frac{\sin(N\omega_p T_p/2)}{N\sin(\omega_p T_p/2)}. \tag{2.20}$$

Here $I(\omega_p)$ is a function with periodic maxima spaced by $2\pi/T_p$ which acts as a frequency filter. Figure 2.11 shows a time and frequency domain pictures of the generation of coherent excitations by multiple pulses.

The force exerted on the system (via the electronic system) is proportional to the optical excitation intensity $I(t)$ [97]. Therefore, the vibrational spectral response of the system should be determined by the Fourier transform of the pulse shape. Several

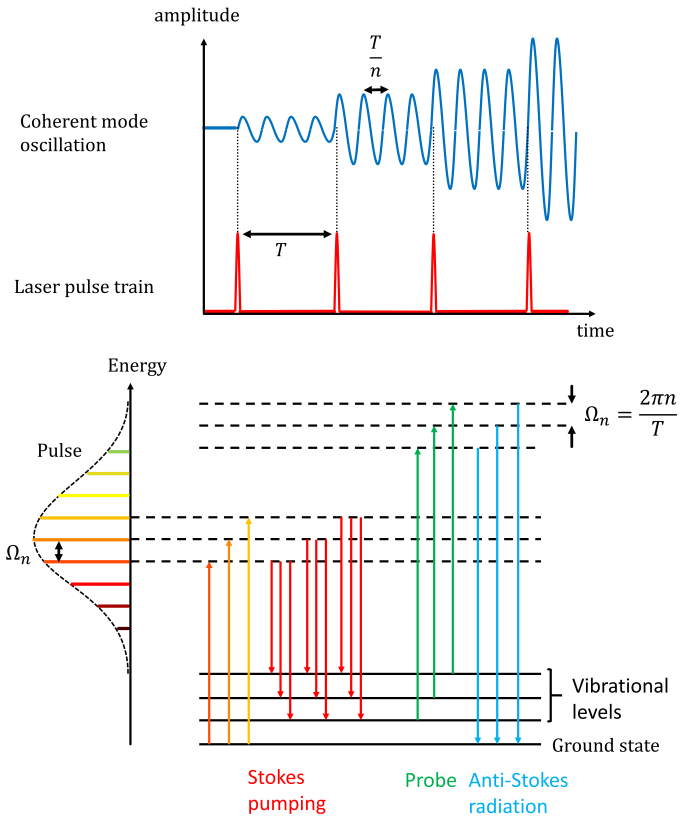

Fig. 2.11 Multi-pulse excitation mechanism. On top the time domain picture. The system is coherently driven at multiples of the laser pulse train period T. On the bottom the frequency domain picture. Impulsive stimulated scattering occurs by the beating of the frequency components of the laser pulse. Here dotted lines correspond to virtual energy states and solid lines to real states.

remarks of interest can be concluded from the above discussion:

1. As the pulse duration approaches the vibrational period T the system impulsive response at this frequency decreases. In fact, even so the pulse bandwidth might exceed Ω, efficient impulsive excitation wont be possible if the temporal structure of the pulse exceeds the vibrational period T_Ω [94].

2. A single pulse with a Fourier-transformed pulse shape might excite all possible vibrational states where the frequencies are lower than the laser bandwidth. In particular, if the system allows it, a continuum of states can be excited by a single pulse.

3. By applying a train of pulses with a time delay between pulses equal to the vibrational period T_Ω, not only the system response at the frequency Ω increases but it will also narrows in bandwidth, *i. e.* the Q-factor at Ω increases with the number of in-phase pulses applied to the system [96].

4. Constructive interference produced by a train of pulses with periodicity T does not only occur at the fundamental mode Ω but also at its harmonics, *i.e.* for the more general condition

$$\Omega_n = n\frac{2\pi}{T}, \tag{2.21}$$

where n is a positive integer number.

5. The amount of sequential pulses N which can be used to pump the system coherently is limited by the dephasing time constant of the state. Let us recall that the state population added in each pulse is independent. The coherence lifetime of an excited state can then be estimated by measuring the maximum number of pulses N at which the response no longer shows amplification due to phase decoherence [95].

2.11 Towards infinite pulsed pumping using frequency combs

From the remarks of Sec. 2.10 it can be concluded that it is desirable to maximize N to allow efficient state pumping with both, a high degree of frequency selectivity and large intensity. The optical creation of such high purity states with large amplitude is of wide interest for modern computing applications, for instance in spintronics and phononics

technologies.

This is not a trivial technological task. Coherent control with $N = 2$ pulses has been used widely since the 80s. Here, typically a Mach-Zender interferometer is employed to create the pulse sequence. In this framework, the escalation of N is achieved by constructing additional interferometers in tandem. This approach rapidly become unpractical for a large values of N. Nelson *et al.* [98] developed an optical scheme capable of delivering a variable repetition rate train of $N = 7$ pulses using a single Mach-Zender type interferometer in a multi-pass configuration. A simpler approach to generate a multipluse excitation has been proposed by Shen *et al.* [64]. In their work, the interference of two chirped pulses was used to generate a variable modulated picosecond pulse, with a variable beat frequency in the sub-THz range. Nevertheless, larger values of N are still a challenge using such pulse shaping techniques.

In this respect, frequency comb (FC) laser sources present a straightforward solution to enhance state pumping selectively by increasing N. FC sources are capable of delivering a practically infinite train of pulses at a fixed repetition rate in the kHz to MHz range. Recently, when commercial frequency combs at GHz repetition rate became available, it has become possible to maximize state pumping in the typical frequency range of acoustic phonons and spinwaves in materials at room temperature (1-30 GHz).

A significant part of this thesis is devoted to the development of an ultrafast pumped Brillouin microscope based on a GHz FC source in order to study the efficiency of coherent pumping using such a scheme for possible applications in non-conventional, high-frequency computing technologies. For this purpose, metallic thin films have been choose as the archetypal systems of study. It is envisioned that properties found in films under repetitive optical stress can be translated to optically-active nano-devices based on those materials.

Besides the benefit of increased acquisition speed by using a high repetition rate source, there are several intriguing physical phenomena which occur when such highly time-structured sources pump quantum systems. When the repetition rate of the excitation and the excited state period are comparable, each pulse raises the state amplitude coher-

ently. But, what happens when the pumping train becomes infinite? It is expected that the system will settle in a steady state. In conventional SBS the sample under excitation is prepared to a coherent state. The inelastic scattering amplitude is then enhanced, but there is no real state pumping because Stokes and anti-Stokes events are equally probable. On the contrary, in the impulsive limit the sample can be truly pumped by the ultrashort excitation. Furthermore, using periodic impulsive pumping, each pulse adds quasi-particles to the population coherently at the laser hot spot. Here, quasi-particle propagation from the pumping spot can be expected. These thoughts entail the creation of a GHz quasi-particle source with a high degree of coherence and amplitude. Moreover, the optical character of such excitation scheme allows the created source to be movable and diffraction limited in size.

CHAPTER 3

Experimental methods

3.1 Outline of the BLS apparatus

This section gives an introduction to the main experimental setup of this work, *i.e.* the BLS microscope system and the femtosecond scanning laser system. For comprehension, a general overview of the technique and the whole instrument is given. The discussion of the details on the design, conception and calibration of the system will follow in section 3.2.

3.1.1 BLS microscope overview

The BLS microscope system consists of a movable holder which positions a sample of interest in between a microscope objective and an electromagnet. The sample is illuminated in a dark field configuration, which allows the observation through a camera for alignment purposes. For laser excitation and probing, the sample is irradiated under the microscope with both, a static probe laser beam at 532 nm and a steerable pump laser beam at 816 nm. Inelastic back-scattering from the probe laser is then collected and filtered out by a spectrum analyser consisting of a tandem Fabry-Perot interferometer (TFPI). The signal is finally read by a photon counter and displayed as the time-integrated Brillouin spectrum of the sample as a function of the $xy-$ coordinates relative to the pump laser position. A complete schematic of the setup is shown in figure 3.1. The main subsystems are divided into: 1) the microscope stage and imaging optics 2) the probe beam optics 3) the interferometer detection and collection optics and 4) the pump beam optics. Light paths are shown in blue, green and red and correspond to

an LED source, probe and pump beams, respectively. Unless otherwise specified, the same nomenclature and color code is used in the following.

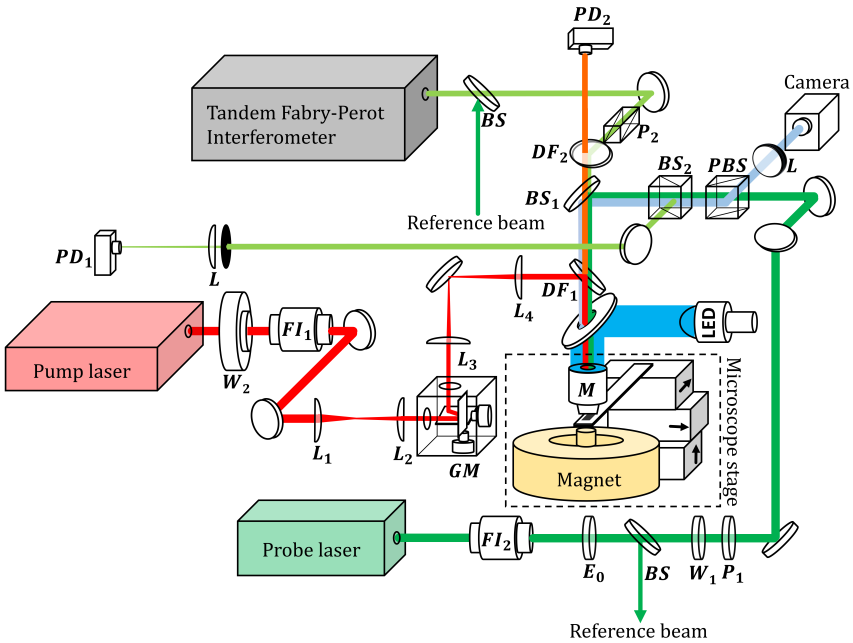

Fig. 3.1 Overview of the full optical system. The different components of the system are referred as follow: BS for beam splitter; PBS for polarization dependent beam splitter; W for waveplate; L for lens; DF for dichroic filter; FI for Faraday isolator; PD for photodiode; P for polarizer; M for microscope and GM for galvo mirror system. The probe, pump and LED beam paths are represented by green, red and blue colors respectively, where dark hues represent the forward paths towards the microscope and light hues the backward paths from the microscope.

3.1.2 Microscope imaging system

The microscope system (see Fig. 3.2) is equipped with a high numerical aperture (N.A. $= 0.75$) objetive (LD EC Epiplan-Neofluar 100x/075) which ensures the submicron lateral resolution needed for the study of nano-structures and nano-devices. The sample is illuminated in a dark field configuration by a collimated LED @470nm reflected by a 45° mirror with a central hole through which light from the microscope travels freely to the imaging optics. This type of illumination provides a very simple method to obtain a

high contrast and high resolution image without the use of a complicated lens system. The sample is held under the microscope by a xyz-nanopositioner which is actively stabilized using image recognition software. Light from the sample is deflected towards the imaging optics by a 10% reflection beamsplitter BS_1 and a 50:50 beamsplitter cube PBS at 532 nm which was selected for its high reflective coating at 470 nm. The image is thus formed in a camera by a tube lens corrected for widefield imaging. A band-pass interference filter F is used to avoid saturation of the camera by the 532 nm probe laser source. This filter is angle-tuned to let pass around 0.1% of the laser light for direct visualization of the laser spot in the camera system. Finally, the image is formed at the camera by an infinity-corrected lens tube L.

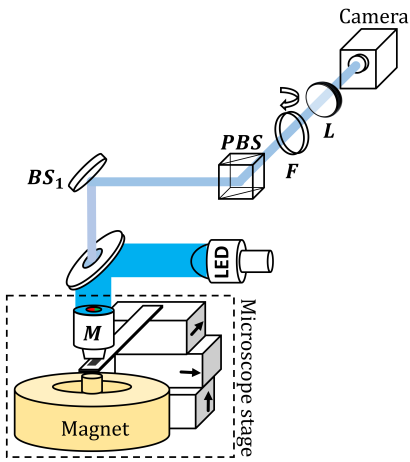

Fig. 3.2 Imaging system diagram. F stands for angle-tuned interference filter; BS_1 for 10% beamsplitter; M for microscope objective; PBS for polarization beamspliter cube; L for lens-tube.

3.1.3 Probe laser system

Figure 3.3 shows a diagram of the probe beam optics. The light source to be used in a BLS experiment is crucial and should meet certain requirements such as high spectral purity and frequency locking. The source chosen is a frequency stabilized diode laser (SpectraPhysics Excelsior One) at 532 nm with a linewidth specification $<$10 MHz and

sidemode suppression of 110 dB. The frequency shift to be measured is in the region 1-10 GHz and the intensity of the signal of interest is of the order of 10^{-12} weaker than the elastic scattering from the sample. Although the interferometer is capable to provide a suppression of 10^{-15} of the elastic peak, it does not suppress spurious side modes from the laser as they overlap with the Brillouin spectrum and appear as a background in the measurement. In order to suppress the sidebands from the laser, a commercial thermally stabilized etalon filter unit (TCF-2 from TableStable LTD) is used. The etalon filter is locked to the main laser peak by a feedback photodiode which controls the temperature of the etalon through a Peltier element. The elaton is decoupled to the laser cavity by a Faraday isolator to avoid flickering. After the etalon, the laser is divided by a beamplitter BS which consists of a uncoated glass wedge. The low intensity reflection from the wedge is used as a reference beam for the interferometer. After the wedge, the main beam is passed through a variable intensity filter constructed by a half-waveplate W_1 and a film polarizer P_1. The beam is thus guided by a periscope mirror set and passed through a polarization beamsplitter cube which selects the p-polarized beam. Finally, part of the beam is reflected toward the microscope objective by beamsplitter BS_1 and the rest is blocked by a beam dump.

3.1.4 The tandem Fabry-Perot interferometer and sample beam optics

The sampling optical system and the TFPI assembly are shown in Fig. 3.4. The TFPI is a commercial unit (TFP-1 form TableStable LTD) and consists of two air-spaced etalons E_1 and E_2. A multi-pass geometry through the etalons is achieved by a retroreflective optical system. The sample beam passes each of the etalons 3 times for a total of six-passes before reaching the detector. The etalons are actively stabilized by five piezoelectric actuators. Four piezos are used to control the parallelism of the etalon mirrors and one piezo is used to stabilized the mirror distance of E_2. A sixth long-travel piezo is used to scan the mirror distance of both etalons simultaneously. The stabilization signal for the piezo actuators is provided by the reference beam collected from the probe laser by beamsplitter BS and is aligned to co-propagate with the scattering beam from the

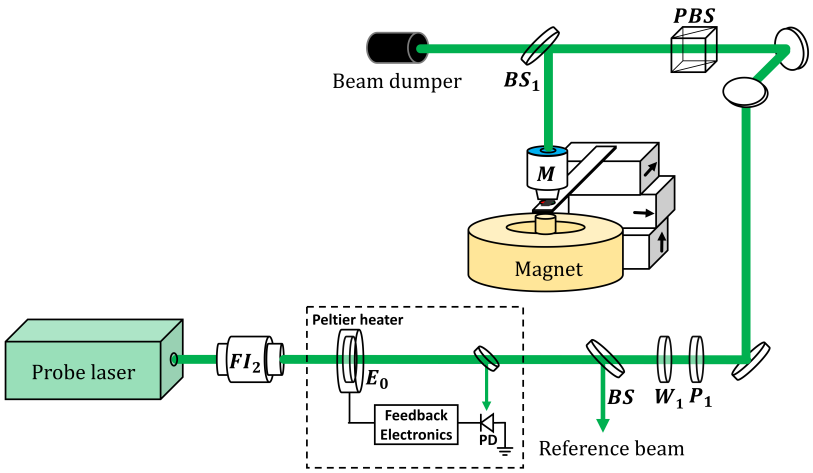

Fig. 3.3 Probe beam optics. PBS stands for polarization beamsplitter cube; W half-waveplate; BS beamsplitter, FI Faraday isolator; P polarizer; M microscope objective; E_0 etalon; PD photodiode. The thermally stabilized etalon sub-assembly is sketched in the dotted-rectangular area.

microscope by an in-built beamsplitter in the TFPI. The Brillouin scattering from the sample is collected toward BS_1 which transmits most of the scattered light. This sample beam is spectral filtered using a narrow bandpass dichroic mirror DF_2 which has a high reflection around 532 nm. The sample beam contains the scattered light from both elastic and magnetic oscillations which is separated by a Glan-Thompson polarizer E_2 before entering the TFPI. The Brillouin spectrum is acquired by scanning the mirror spacing of the TFPI and by integrating the transmission of the interferometer with an avalanche photodiode (APD).

3.1.5 Scanning microscope system

Collective oscillations are induced at the sample by a high repetition rate fs laser source. This source, hereafter referred to as the pump laser, consists of a commercial 1 GHz Ti:Sapphire laser (LaserQuantum TaccorPower) with a 30 fs Fourier limited pulse duration. The laser is extremely sensitive to back reflections into the cavity which causes the laser to lose mode-locking. To prevent this, a broadband Faraday isolator FI_1 is

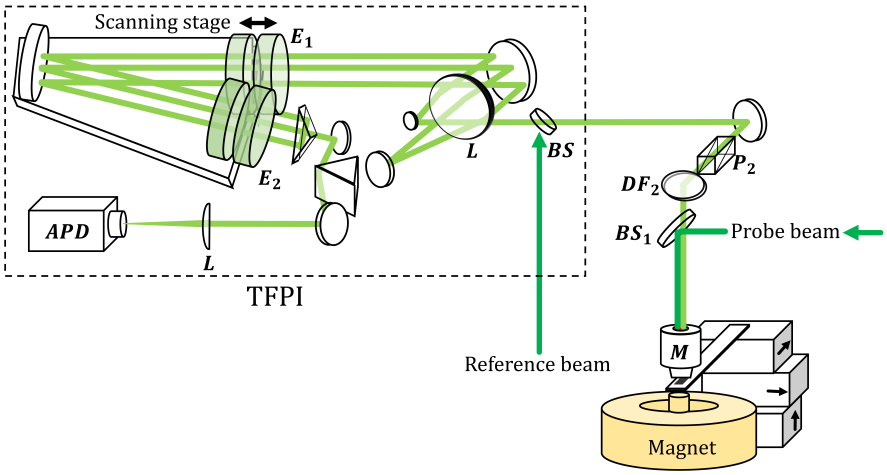

Fig. 3.4 Sample beam optics and TFPI internal optics. BS stands for beamsplitter; DF dichroic beamsplitter; P Glenn-Thompson polarizer; L lens; M microscope objective; E_0 etalon; APD avalanche photodiode.

placed before the scanning optics. The isolator is used together with an achromatic half-waveplate W_2 to control the intensity of the laser beam. The half-waveplate is mounted in a motorized rotation stage which is used for automatic measurements against laser power.

The scanning system (see Fig. 3.5) is built after the Faraday isolator and consist of a $4f$ lens system and a pair of motor controlled 1-dimensional mirror galvanometers. The first two lenses of the scanning system have focal lengths of 100 and 50 mm and form an intermediate image plane at the center of the galvanometer mirrors. The following pair of lenses have focal lengths of 100 and 150 mm and are placed so that the previous image plane formed at the center of the mirror galvanometers and the back entrance of the microscope objective become conjugate planes. In this setup, the mirrors galvanometers raster scan the pump beam across the sample in the $x-$ and $y-$ directions. The pump beam, the probe beam and the LED light are merged by a dichroic beamsplitter filter DF_1 which reflects the fs laser and transmits the other light sources. Backscattered light from the sample is transmitted by DF_1 and collected by a photodiode PD_1 for calibration purposes.

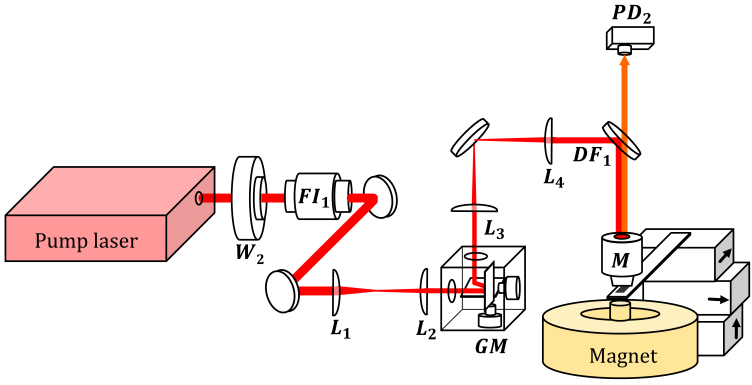

Fig. 3.5 Pump beam optics schematic. GM stands for mirror galvanometer; W half-waveplate; DF dichroic beamsplitter, FI Faraday isolator; P polarizer; L lens; M microscope objective; PD photodiode.

3.1.6 Data acquisition and automation architecture

The whole apparatus, including all subsystems, is controlled by a grid computing set (see Fig. 3.6) consisting of 3 CPU units connected together via network. Each subsystem from the BLS microscope is connected to the computers either by a serial port connection or trough a data acquisition card (DAQ). Individual software for control and automation of each subsystem was written separately in a set of Labview VIs (virtual instruments) which include calibration routines, diagnosis, reading variables and controls. The communication engine between the different VI's is provided by a commercial package (THATec:OS platform) which includes all software and network connections to a main graphical user interface (THATEC:OS GUI). The GUI connects all VIs together via a transmission control protocol (TCP). The GUI displays all control and indicator variables programmed in each sub-VI and allows the graphical programming of automatic measurement loops using any range of this variables and the corresponding data display. The addition of new software is thus made by programming individual standalone software and the integration is made by using the THATec:OS core package.

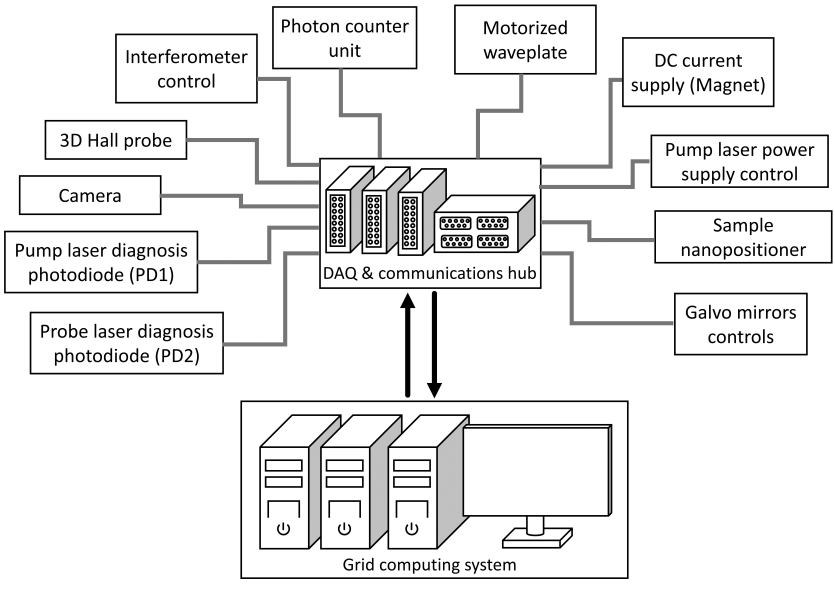

Fig. 3.6 System hardware architecture. The software architecture follows a similar topology; standalone control software for each hardware subsystem is controlled by the main GUI (hub).

3.2 Optical and hardware design of the frequency comb Brillouin microscope

The BLS microscope core is based originally on a design made in the University of Perugia and a complete characterization and specifications of such system may be found elsewhere [27]. The first version of the BLS microscope was designed to use a physical contact method to induce collective oscillations in the sample while using an optical method to probe the excitation. In this work, I demonstrate an ultrafast optical method using a high repetition rate laser can induce and characterize collective excitations selectively without the need of an electrical contact built into the sample. This section presents a discussion on the system concept, the optical design, the technical specifications, and calibration methods of the new instrument.

3.2.1 Ultrafast laser source

The frequency range of interest for spinwaves in ferromagnetic materials is typically between one and a few tens of GHz for moderate magnetic fields ($<$1 Tesla). There are two different technologies of commercially available mode-locking lasers that are able to reach such high repetition rates. The first type is based on a fiber oscillator with available repetition rates up to 250 MHz out of the box. A mode-locking fiber laser offers a compact and robust solution with high wavefront qualities. Output powers directly from the fiber oscillator can reach up to 100 mW and have typical pulse durations in the range of 50-150 fs. Higher repetition rates are achieved by the implementation of multiplication Fabry-Perot cavity filters [99]. With this method, repetition rates up to 25 GHz have been reported [100], starting from a 250 MHz laser source. In practice, Fabry-Perot filters places a very high demand on the finesse to efficiently suppress spurious pulses at the original repetition rate of the source. The coupling efficiency of such high-finesse multiplication cavities is very low and the output power of a laser source of several Watts barely surpass a few mW after filtering. Nevertheless, an advantage of a fiber-based laser source is its exceptional beam profile quality, which allows the

beam to be efficiently coupled to external fiber amplifiers that can increase the power by several orders of magnitude. A drawback by the use of external optical amplifiers is the degradation of the laser spectrum after the amplification where a typical pulse duration is rarely less than 120 fs after compression. At the end, the addition of cavity filters, amplifiers and a compression unit required to reach GHz speed of the ultrashort pulse train turn the system into a more bulky and complex device than the original fiber oscillator.

The second type of commercial source able to reach the experimental requirements is based on solid-state laser technology. Ti:sapphire lasers are the most common sources of ultrashort pulses with high average power and repetition rates up to 10 GHz. Moreover, with the development of diode pumping, this type of laser is nowadays available as a compact turn-key operation device without the need of a bulky Argon Ion or Nd:Yag pump laser. The drawbacks of these systems are the beam ellipticity and astigmatism that is characteristic of the small laser cavities needed to reach GHz repetition rates. As an example, according to the manufacturer specifications the M^2 of a 1 GHz laser cavity is 1.2 while for a 10 GHz oscillator the M^2 is 1.5, making this type of lasers impractical for fiber amplification. However, as the typical pulse duration of these systems is of around 30 fs and have average powers of several watts directly out of the laser cavity without the need of extra optics or compression, this solution is more convenient and elegant than a fiber based source.

The laser purchased for this project was a 1 GHz repetition rate Ti:sapphire oscillator from LaserQuantum (TaccorPower model). Table 3.1 summarizes the specifications of this laser measured in our laboratory directly after delivery.

3.2.2 Optical design of the laser scanning system

Conventionally, a laser scanning microscope uses a pair of small mirror galvanometers (GM) close together to pivot the beam optical path and a system of lenses to image the pivoting plane at the entrance aperture of the microscope objective. In this way,

Parameter	measured value
M^2 sag. plane	1.09
M^2 tan. plane	1.04
Ellepticity[1]	1.23
Divergence	1 μrad
Wavelength	816 nm
Bandwidth	28 nm
Pulse duration	29.75 fs
Power	2 Watts
Power stability	0.4%

Table 3.1 Laser specifications measured in the laboratory. [1]Measure 60 cm away from the output port

a net lateral displacement of the laser focus in the sample plane after the objective is achieved by steering the galvanometers. The general requirement to be fulfilled by the scanning optical system is to keep the filling factor of the objective by the laser constant regardless of the steering angle. Such a condition is needed in order to maintain the pumping energy fluence and the spot characteristics constant at the sample plane while the scanning is performed.

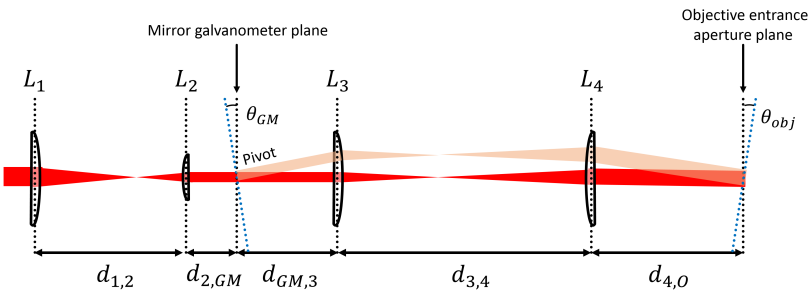

Fig. 3.7 Unfolded optical layout of the scanning mechanism. L stand for lens;d stand for distance. The mirror galvanometer and the objective entrance aperture plane are conjugate focal planes.

The design followed here consists of a double afocal optical system formed by four lenses, as shown in figure 3.7. Lenses L_1 and L_2 compose the first afocal system. The second afocal system composed by lenses L_3 and L_4 is positioned such that it forms conjugate planes at the entrance aperture of the microscope and the center of the mirror galvanometers (GM plane). The arrangement of lenses L_3 and L_4 which satisfies the

previous condition are easily calculated from the thin lens formalism with the equations

$$d_{3,4} = f_3 + f_4, \tag{3.1}$$

$$d_{GM,3} = \frac{f_3}{f_4}\left(f_3 + f_4 - \frac{f_3}{f_4}d_{4,O}\right), \tag{3.2}$$

where f_3 and f_4 are the focal distances of lenses L_3 and L_4 respectively and the distances are as shown in Fig. 3.7. Equation 3.1 is the afocal condition of the second system while Eq. 3.2 relates the position of the conjugate planes of the system with respect to L_3 and L_4. Therefore, as shown in 3.7, steering of the laser beam by the mirror galvanometers produces a pivot around the entrance aperture of the objective without lateral displacement of the spot position. The tilting angle θ_{GM} at the GM plane is related to the pivoting angle θ_{obj} at the objective entrance aperture plane by

$$\theta_{obj} = -2\left(\frac{f_3}{f_4}\right)\theta_{GM}. \tag{3.3}$$

At the sample plane, the displacement of the laser spot r for a given steering angle θ_{GM} is related trough

$$r = f_{EFL}\theta_{GM}, \tag{3.4}$$

where f_{EFL} is the effective focal length of the microscope objective. The first afocal system formed by L_1 and L_2 has the function of steering the beam along the $z-$direction (normal to the image plane) and to displace the focal plane of the pump laser. A shift in the pump focal plane under the microscope can be used to effectively modify the pumping area up to several micrometers in diameter or to correct for the shift between the probe and pump focal planes arising from the different divergences of the two beams. In the paraxial approximation, the size of the spot h_{GM} at a distance $d_{2,GM}$ after L_2 is given by

$$h_{GM} = \left[\frac{(d_{1,2} - f_1)(d_{2,GM} - f_2)}{f_1 f_2} - \frac{d_{2,GM}}{f_1}\right]h_{laser}, \tag{3.5}$$

where h_{laser} is the laser spot size before L_1 and f_1, f_2 the focal distance of lenses L_1 and L_2, respectively.

It is now clear that if $d_{2,GM}$ is chosen to be equal to the focal distance of the second lens f_2, Eq. 3.5 is reduced to

$$h_{GM} = -\left(\frac{f_2}{f_1}\right) h_{laser}. \tag{3.6}$$

Equation 3.6 shows that if the distance from the GM plane to L_2 is equal to f_2 the spot size of the laser beam at this plane is constant regardless of the distance between the lenses $d_{1,2}$. Hence, by small displacement of lens L_1 some divergence or convergence is added to pump beam without affecting the filling factor of the objective. The focal plane shift Δz generated by a displacement of the first lens $\Delta d_{1,2}$ is related by the optical system parameters as

$$\Delta z = \left(\frac{f_3}{f_2}\right)^2 \left(\frac{f_{EFL}}{f_4}\right)^2 \Delta d_{1,2}. \tag{3.7}$$

Finally, the magnification of the scanning lens system is given by

$$M = \frac{f_4}{f_3}\frac{f_2}{f_1}. \tag{3.8}$$

3.2.3 Practical construction of the scanning optics

The first consideration for the choice of the lenses focal distances and the geometry of the optical system was based on the physical constraints forced by the fixed position of the objective in the BLS microscope, the position of the probe beam laser optics, the pump laser optics and the whole frame of the microscope. A second consideration was the compromise between the compactness of the system and avoiding excessively large optical aberrations from the lenses. The design was first built virtually using a CAD program from calculations applying the thin lens equations presented in the previous section. A render image of the optomechanical system is presented in figure 3.8. Table 3.2 summarizes the chosen parameters of the system.

Parameter	value
f_1	100mm
f_2	50mm
f_3	100mm
f_4	150mm
f_{EFL}	150mm
$d_{GM,3}$	100mm
$d_{4,O}$	50mm
M_T	0.75

Table 3.2 Lens design parameters.

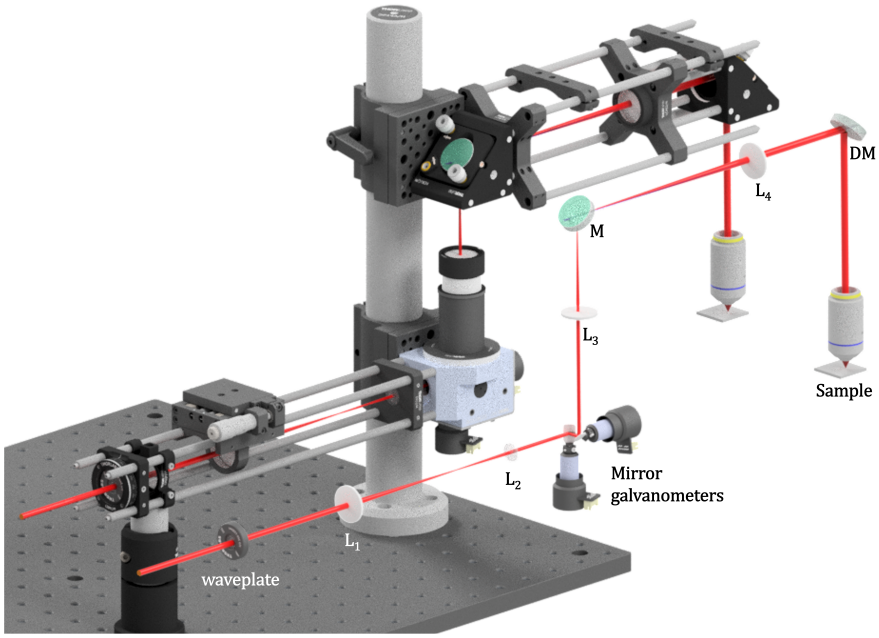

Fig. 3.8 Optomechanical CAD design on the scanning laser optics.

Lenses ratios were chosen such that the transverse magnification M_T adjusted the beam size of the laser to the entrance aperture size of the microscope. From the values from Table 3.2, other parameters can be calculated. For example, in the mechanical design the displacement of lens L_1 is fine adjusted by a $\Delta d_{1,2} = 12.7$ mm travel micrometer stage. This displacement corresponds to a shift in the focal plane of $\Delta z = 36.12$ μm. The resolution is mainly limited by the precision, repeatability and thermal stability of

Parameter	value
repeatability	15 μrad
resolution	15 μrad
thermal drift	10 μrad/°C

Table 3.3 Galvanometer specifications from the manufacturer.

the galvanometer motors. Table 3.3 shows the specification of this parameters given by the manufacturer.

With the system parameters chosen according to Table 3.2, the displacement resolution of the scanning system is estimated to be 80 nm and with a maximum thermal drift of 53 nm per °C. Equations 3.3 and 3.4 show that it is possible to increase the resolution of the system and reduce the thermal drift effect by decreasing the ratio f_3/f_4. This however introduces another complication; since the two galvanometers for steering in the $x-$ and $y-$ directions are separated by some millimeters, the $x-$ and $y-$ steering planes are shifted. Thus, there are two different image planes that fulfill the stationary condition, one for each direction, but there is not a true single plane that fulfill this condition simultaneously for both directions. For small steering angles this difference is unnoticed. But as the ratio f_3/f_4 decreases, the ratio θ_{GM}/r increases and larger steering angles are needed to scan the beam. As a consequence the effect of the offset in the $x-$ and $y-$ steering planes becomes more prominent. The focal lengths from Table 3.2 were chosen so as not to compromise the scanning stiffness for resolution and vice-versa.

Finally, the type of lenses and materials are chosen. In the literature L_3 is referred as the scan lens and L_4 referred as the tube lens in an scanning system. Conventionally, achromatic doublets are chosen for these two lenses. Achromats reduce chromatic aberrations which is important in multiphoton microscopy where typically laser pulses $>$120 fs. However, the high-dispersion materials used in this type of lens are not suitable for laser pulses with a duration of the order of 30 fs, which is the case for our system. Hence, ultra-thin fused silica lenses were chosen for the design. An estima-

tion of the dispersion of these two cases was done using a commercial software tool (vCHRIP from LaserQuantum). As an example, in figure 3.9 the dispersion of a pair of acrhomats from Thorlabs, AC254-100 and AC254-150 was analyzed using vCHIRP and compared to the dispersion of two ultrathin fused silica lenses from EksmaOptics, 110-1211ET and 110-1217ET. The input spectrum is a gaussian pulse of 30 fs and central wavelength at 816 nm to imitate the characteristics of the laser used in this work. It was concluded that fused silica ultra-thin lenses elected for the optical system stretches the pulse to around 42 fs, corresponding to the dispersion of 9 mm of the material, while the alternative option of achromatic doublets would stretch the pulse to around 300 fs.

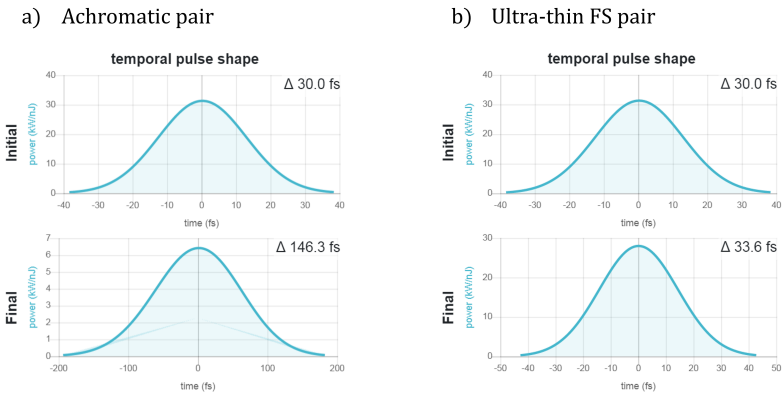

Fig. 3.9 Pulse duration before and after passing the sacanning system consisting of: a. A pair of achromatic lenses from Thorlabs and b. A pair of ultra-thin fused silica lenses from EksmaOptics.

3.2.4 Construction of the microscope optics

The imaging system and the probe laser guiding optics were built with cage optomechanics. Figure 3.10 shows the CAD design of the platform. A view of the interior optics is shown in figure 3.11. The nomenclature matches that of figure 3.1. The system geometry is defined by the cage axes, which makes the alignment simple and robust. The complete system together with the scanning microscope is shown in figure 3.12.

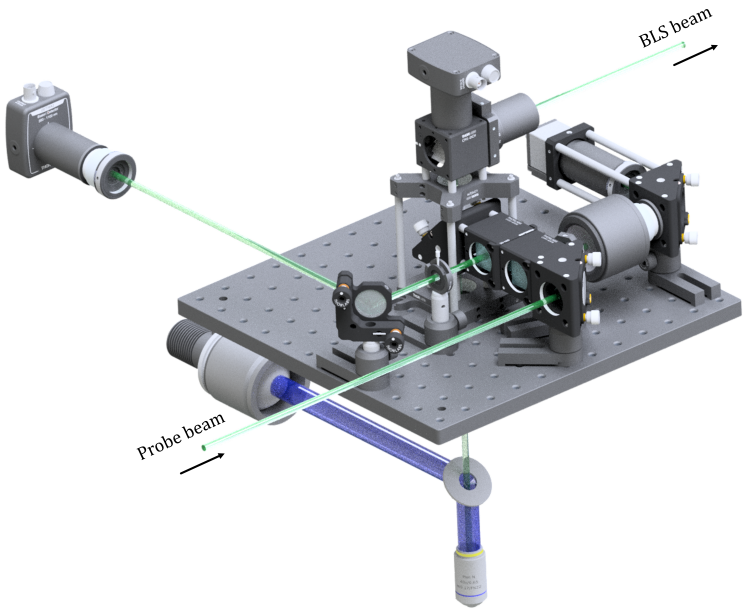

Fig. 3.10 Optomechanical CAD design of the microscope and probe laser optics.

3.2.5 Calibration of the laser system

After optimal alignment of the scanning optics, the displacement of the laser beam at the sample plane as a function of the voltage applied to the galvanometer motors was calibrated. For this procedure, a dedicated calibration target was prepared. The target was produced by high resolution electron beam lithography on a sapphire substrate and consists of a Pt grid of 5 μm width and 20 nm thickness. Figure 3.13b shows a scanning electron microscope (SEM) image of the calibration target. The sample target was carefully aligned under the microscope and the laser beam was focused at the sample plane. Each galvanometer mirror is raster scanned across the Pt pattern separately. A weak back reflection from the sample is collected after the dichroic filter DM_2 and focused on to photodiode PD_2 by a lens. As the laser is scanned in one direction across the Pt grid the reflected intensity varies periodically (see Fig. 3.13a). The reflected signal is acquired in a 40 μm range in steps corresponding to an applied voltage of 0.1 mV to the galvanometer motor and then differentiated. The derivative of the reflection

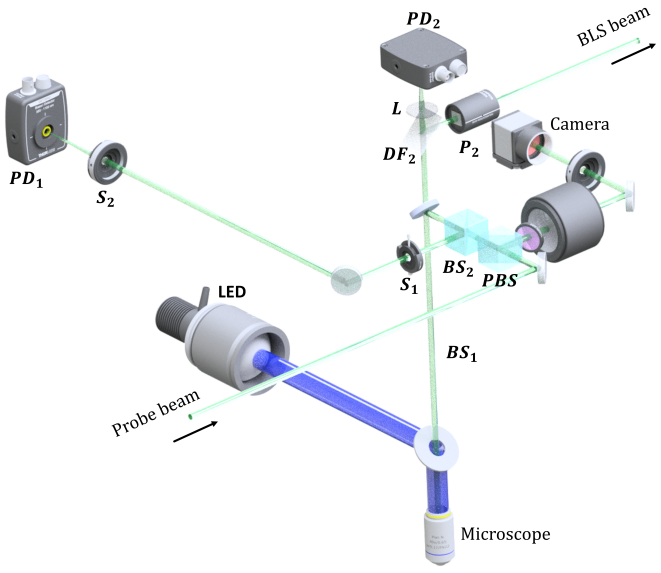

Fig. 3.11 Interior optics from figure 3.10.

signal has equally spaced maxima and minima corresponding to the edges of the target grid separated by 5 μm. Knowing this, two extreme maxima are taken as a reference and the corresponding distance between them calculated from the number of periods in the plot. The same procedure is followed for the other motor in the orthogonal direction.

3.2.6 Microscope active stabilization

BLS measurements, especially 2D Brillouin images, are exceedingly time consuming. To avoid drifting from the measurement position and defocus from the sample surface an active stabilization system is used. The focal position is stabilized by sampling the Rayleigh back-reflection from the sample by a photodiode (PD_1) far away from the microscope. Two limiting apertures (S_1 and S_2 in figure 3.11) of 3 mm diameter separated by 2 meters were placed to define the beam path between the microscope and the photodiode. A 100 mm focal length lens focuses the light onto the photodiode and the intensity is controlled by a film polarizer to increase the dynamic range below saturation. The sample stage is scanned in the $z-$direction and the back reflection intensity

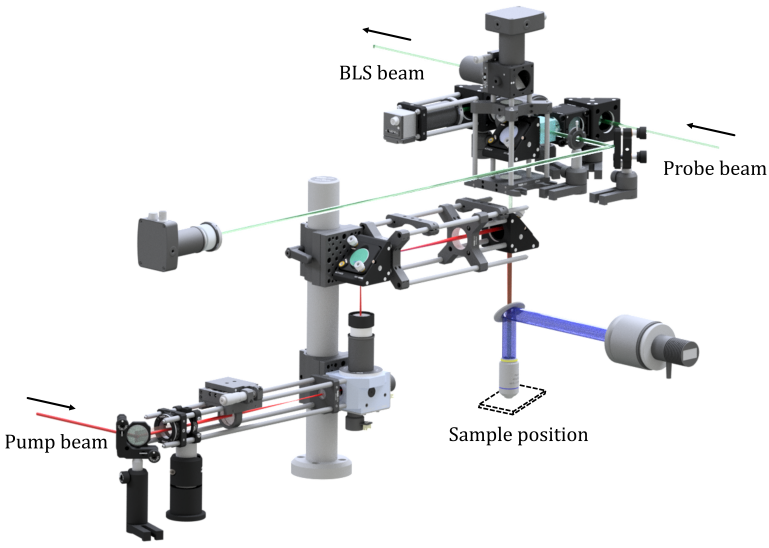

Fig. 3.12 Complete laser microscope CAD design.

as a function of the stage position is measured by the photodiode. The reflection is divergent for all values of z except for the focus condition in which the reflected beam is fully collimated. The two limiting apertures ensure that the maximum transmission to the photodiode occur only when the sample is at the focus of the microscope. The nanopositioner has an in-built servo-loop and a PID-controller feedback which is seen by the photodiode as an oscillating background. In order to remove this background and other ringing effects from the stage while the stage is searching for the focus position, a low pass filter with cut-off frequency at 15 Hz was constructed and used to condition the signal from the photodiode. The focus position is then found by fitting a parabolic profile to the intensity read by the photodiode as a function of the stage $z-$coordinate. The stabilization in the $x-$ and $y-$axes is done by commercial software which performs a pattern recognition algorithm on the microscope image. During long term measurements, active stabilization is always on to prevent the probe area from drifting.

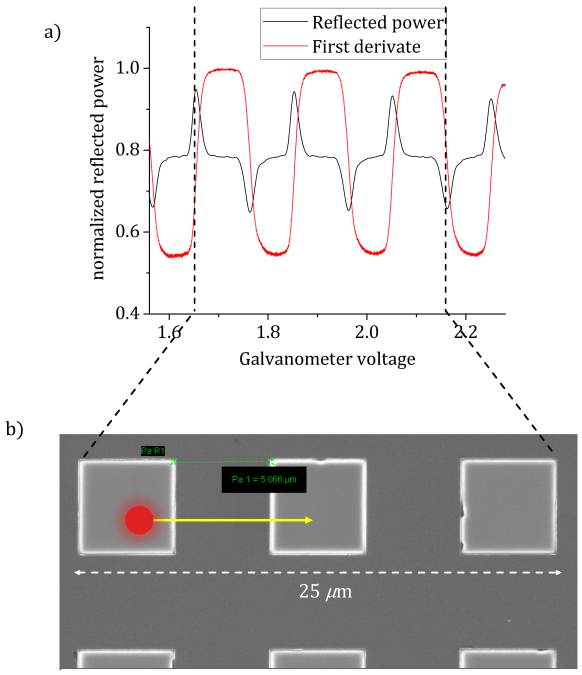

Fig. 3.13 a. Reflected power as a function of the applied voltage to one of the galvanometers. b. SEM image of the target. The yellow line shows the direction of the scanning.

3.2.7 Lateral spatial resolution of the laser microscope

The resolving power of the system is given by the spot size of the probe beam under the microscope objective. Similarly, the optical pumping spatial resolution is given by the pump beam spot size. To determine the spatial resolution of both lasers a knife edge measurement [101] of the spot size was performed. This was done by scanning the beams across one of the edges of the Pt calibration target and acquiring the reflectivity of the pump and probe beams with photodiodes PD_2 and PD_1, respectively. Assuming that the intensity profile of the laser is a gaussian distribution, the reflected power measured by the photodiode while the laser is scanned across the Pt edge is given by

$$P = P_0 + \frac{P_1}{2}\left(1 - \mathrm{erf}\left(\frac{\sqrt{2}(x - x_0)}{\omega}\right)\right), \tag{3.9}$$

where P_0 is a background offset, P_1 is the maximum reflected power, x_0 is the position at which the power drops to half its value, erf is the gauss error function and ω is the beam waist. Fig 3.14 shows the reflection power of the probe beam at the best focus and the fit of Eq. 3.9 from where a beam waist of 310 nm was obtained.

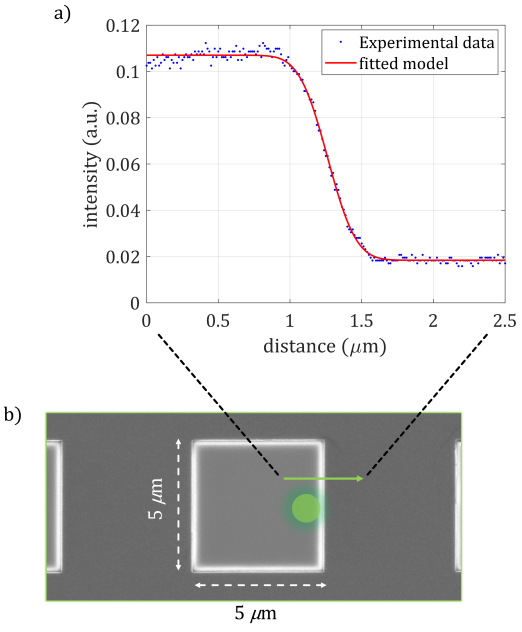

Fig. 3.14 a. Reflected power versus relative position of the Pt edge. b. SEM image of the calibration target. The green arrow represents the direction of the scan.

The probe beam is assumed to be stigmatic, and therefore only one measurement is required to determine the beam waist. In the case of the pump beam, two issues are apparent. First, the beam is astigmatic and therefore a characterization in the two axial directions should be performed. Secondly, the exact focal position of the beam is unknown a priori and needs to be matched with the probe beam focal plane. In order to match the pump and probe focal planes a measurement of the beam waist was performed for different positions of lens L_1 while maintaining the focus stabilization of the microscope activated. The measured beam waist against $d_{1,2}$ reassembles the propagation of a gaussian beam and is described by

$$\omega = \omega_0 \sqrt{1 + \left(\frac{z - z_1}{z_0} \right)^2}, \tag{3.10}$$

where z is the displacement of L_1, ω_0 is the minimum beam waist, z_1 is the position at which the beam waist is minimum and z_0 is a parameter called Rayleigh's range. To perform this measurement, L_1 was set in the middle range of the lens micrometer stage positioner and $d_{1,2}$ was set equal to $f_1 + f_2$ which corresponds to the $z = 7$ mm in figure 3.15. The minimum waist of the two axial directions obtained from the fit of Eq. 3.10 to the experimental data of figure 3.15 was 690 $\pm$ 77 nm and 742 $\pm$ 69 nm, respectively. The two astigmatic planes were found for position of L_1 corresponding to $z = 6.94 \pm 0.3$ mm and 6.69 ± 0.22 mm. Lens L_1 was thus set at $z = 6.85$ mm and the resolution estimated to be better than 800 nm.

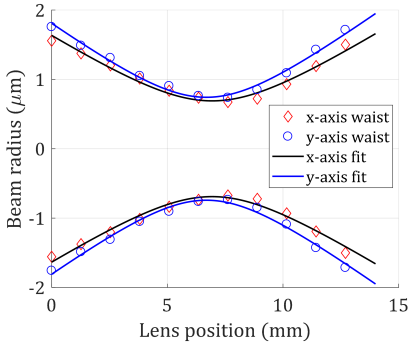

Fig. 3.15 Beam radius as a function the micrometer stage position.

3.3 Alternative detection platforms

In this section, two alternative Brillouin setups are presented. The first alternative is based on optical analysis using a commercial VIPA spectrometer. The second alternative presented is based on broadband electrical detection using a high-speed photodiode and a vector-network analyser (VNA).

3.3.1 A VIPA-based Brillouin microscope

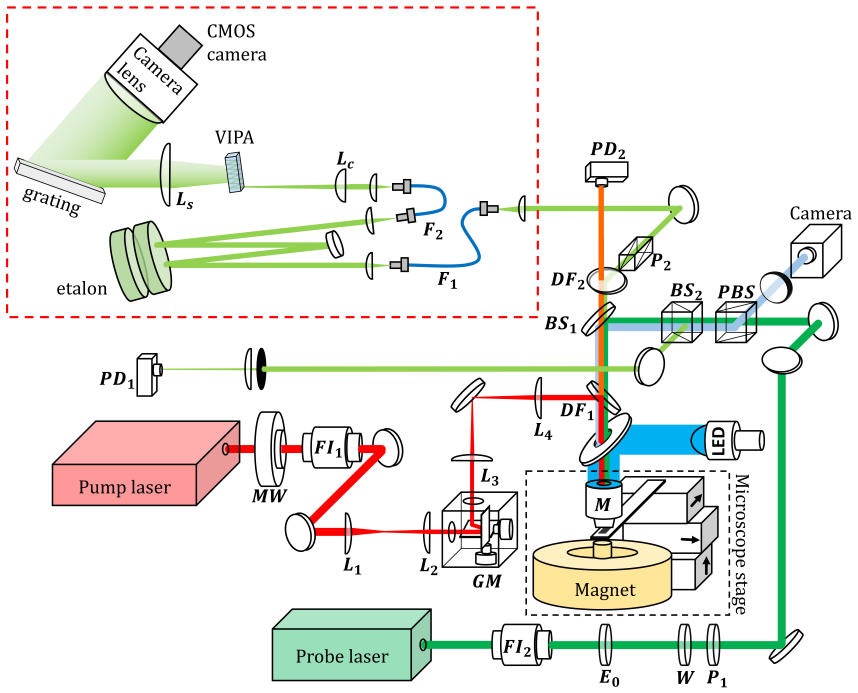

Fig. 3.16 Experimental setup. The red dotted rectangle shows the VIPA spectrometer arrangement. F_1 is the coupling fiber to the spectrometer, F_2 is a fiber link which connects the suppression filter with the dispersive block. The elements L_c and L_s correspond to a cylindrical and an spherical lens, respectively. All other lenses shown in the VIPA setup are aspherical collimation lenses. The rest of the elements in the schematic follow the nomenclature from Fig. 3.1.

The first alternative implemented in this work to replace the TFPI unit was a novel VIPA spectrometer. Such spectrometers have been very successful in biomedical re-

search [76, 102–104]. Despite this success, until the time of this work there had not been any implementation of such kind of spectrometers to solid state magnetism research, perhaps because the surface scattering due to spinwaves in metallic compounds is far weaker than what it is obtained from bio-materials.

The VIPA spectrometer used in this work was a demonstration commercial unit (Brillouin Hyperfine spectrometer from LightMachinery). The VIPA experimental setup reuses the FC-BLS microscope presented before in this chapter with the difference that here the TFPI has been replaced by the VIPA spectrometer. Figure 3.16 shows an schematic of the VIPA-based Brillouin microscope.

The VIPA setup consists of two main blocks connected by an optical fiber (F_2), namely, an etalon filter block and a dispersive block which contains the spectral analysis optics. The spectrometer input requires a single-mode fiber coupling connection (F_1). The filter block consists in a double pass air spaced tuneable etalon which achieves a suppression of around 10-15 dB per pass. The filtered light is then coupled to the fiber F_2 and guided to the dispersive block. This block consist of several lenses, a VIPA element, a grating, a camera lens and a high resolution CMOS camera sensor. The light beam coming from fiber F_2 is collimated and then focused by a cylindrical lens into the VIPA element. The FSR of the VIPA in this unit was 75 GHz. The output after the VIPA is the spectrum of the light source folded in a single FSR. After the VIPA a grating is used to separate each FSR laterally into a ~ 3 THz spectral range. A camera lens is used to focus the dispersed light into a high resolution CMOS camera where a 2-dimensional (2-D) spectrum is acquired as an image.

The 2-dimensional spectrum is formed by a linear grid in which each line correspond to a part of the spectrum and has a length equal to 1 FSR. The linear grid is then folded by software into a 1-dimensional spectrum. Figure 3.17 shows an example of the raw acquisition of the camera sensor and the 1-dimensional folded spectrum by the spectrometer software. Here a broadband LED source was coupled to the spectrometer fiber which served for alignment of the double pass etalon filter and calibration of the spectrometer. The spectrum in Fig. 3.17 is the reflected spectrum of the double passed

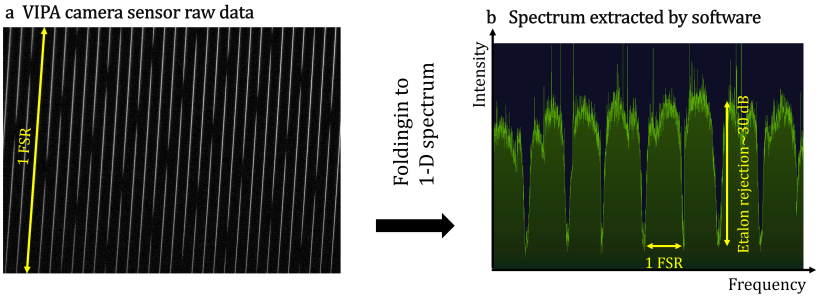

Fig. 3.17 Hyperfine display of the etalon filter transmission. a. Spectrum of a LED broadband source. Each diagonal line correspond to one FSR (75 GHz). **b.** Spectrum after software folding into one dimension. The lateral distance between intensity dips correspond to 1 FSR. The depth of the dips correspond to ~ 30 dB.

etalon. In Fig. 3.17a the empty spaces in the linear grid (dips in the 1-dimensional spectrum in Fig. 3.17b) correspond to the rejection band of the etalon filter. The suppression filter width is specified by the manufacturer to be 500 MHz.

3.3.2 FR-MOKE microscope

The FR-MOKE alternative is a novel technique which is based on an electrical rather than optical analysis. This setup exploits the MOKE, which modulates the polarization of scattered light at the Brillouin frequency f_0. The modulation in the polarization is then converted into an intensity modulation by a polarizer set at 45° with respect to the beam polarization main axis. After the polarizer the intensity modualtion of the beam is < 1 pW. A high-speed 40 GHz bandwidth fiber-coupled GaAs photodetector (model 1004 from Newport) is used to convert the optical stimulus into an RF electrical signal which is modulated at the Brillouin frequency. The electrical signal is then spectrally analyzed by a VNA unit (model ZNB-40 from RohdeandSchwarz).

This setup was built using the main body of the BLS microscope with the difference that the TFPI has been replaced by a photodetector coupling assembly, which consists only of a 3-axis fiber launcher. Figure 3.18 shows the schematic of the experimental setup. Note that the optical system is shown simplified in this schematic to put more emphasis on the electrical system. Although we have used the full BLS microscope

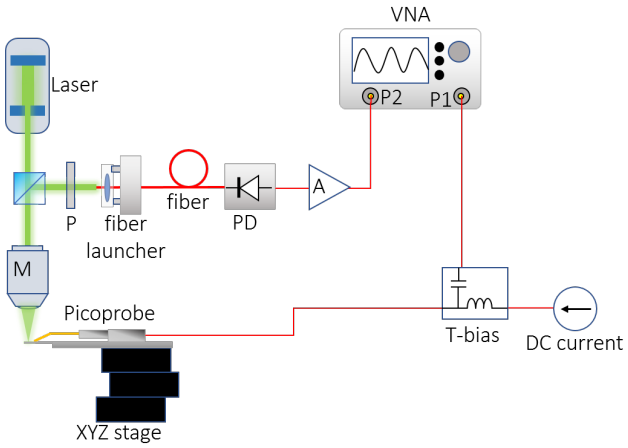

Fig. 3.18 FR-MOKE experimental setup. The optical setup is shown simplified to only the essential elements. Green glow lines represent laser paths. Red thin lines represent electrical connections. P- polarizer, M- microscope objective, PD- photodiode, A- amplifier.

facility, and contrary to the TFPI and VIPA detection schemes, this technique does not require a highly specialized probe laser system and most optical elements from the original BLS microscope are actually redundant. Instead, this method requires the sample to be driven coherently in resonance with a referenced source and an additional RF circuit is needed to stimulate the sample electrically. Both the reference stimulus and the detection are executed by the VNA at the same frequency via port 1 and port 2, respectively. The stimulus signal is fed to the sample via a two-contact microwave testing picoprobe (from GGB Industries Inc.) which is physically connected to the sample. This setup was build to study spin-Hall nano-oscillaors (SHNOs), which require a DC current to operate. For this purpose a DC current is added to the VNA stimulus using a T-bias connector. On the detection side, a 70 dB RF amplifier (Model AFS44-020018 from Miteq) is used to amplify the signal coming from the photodiode above the noise floor level of the VNA.

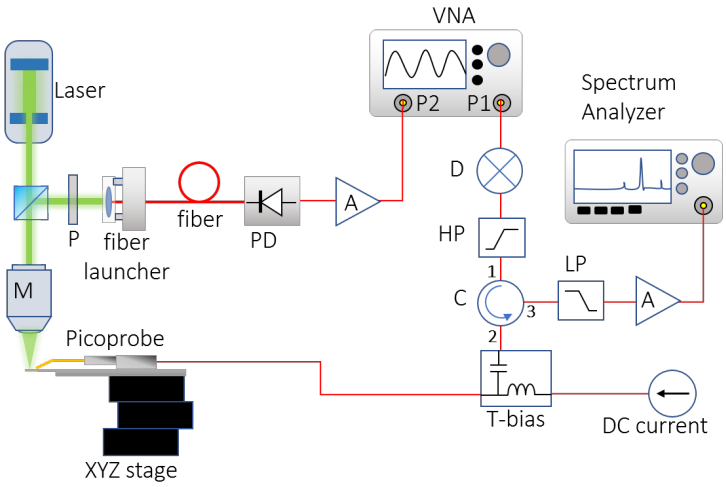

Fig. 3.19 FR-MOKE experimental setup. The optical setup is shown simplified to only the essential elements. Green glow lines represent laser paths. Red thin lines represent electrical connections. P- polarizer, M- microscope objective, PD- photodiode, A- amplifier, D- frequency doubler, HP- high-pass filter, LP- low-pass filter, C- circulator.

3.3.3 Second-harmonic pumped FR-MOKE microscope

Coherent driving can be performed in resonance at the second harmonic $2f_0$. In this scenario the frequency of the oscillator f_0 has the possibility lock either in the first or in the second cycle every two $2f_0$ cycles, thus allowing two different locking states, each with a $180°$ phase difference. This bi-stable framework is of interest in many spintronics applications as for instance, phase-binarization and neuromorphic computing [105].

The schematic of the setup is shown in Fig. 3.19. The optical assembly and the detection path (VNA Port 2 connection) is the same as shown in Fig. 3.18. In Port 1, a supplementary circuit has been added to generate the stimulus at $2f_0$. The VNA operates at the test frequency f_0 (stimulus) in both ports. Therefore, an active RF frequency doubler (Model AKKa-2X from Spacek Labs) is used to multiply the reference stimulus to $2f_0$. A high-pass filter with 100 dB insertion loss at 7 GHz (Model ZHSS-K15G+ from MiniCircuits) is connected right after the doubler to completely suppress the fundamental frequency from the stimulus. After the filter the stimulus is sent through a 3-ports circulator, whose purpose will be explained in the next paragraph. Subsequently,

the $2f_0$ stimulus is mixed with a DC current bias trough a T-bias. The combined DC/RF stimulus is then fed to the sample through the picoprobe.

Since the stimulus is at $2f_0$ and the sample response is at f_0, it is possible to read the pump-free electrical signal reflected from the sample trough the picobrobe. The reflected signal is guided backward all the way to the circulator where it is directed on a third path (port 3 of the circulator in Fig. 3.19). After the circulator, the excessive RF power at $2f_0$ is removed with a low pass-filter (ZLSS-11G-S+ from Minicircuits). Afterwards, the signal is amplified with a 70 dB RF amplifier (Model AFS44-020018 from Miteq) and the power spectrum is acquired with an spectrum Analyzer.

This setup allows simultaneous optical an electrical measurements of a locked oscillator. While the electrical measurement provides a fast monitoring of the overall state of the oscillator, the optical measurement provides a phase-resolved measurement of the local properties of the device. This setup also allows the electrical characterization of free-running oscillators (no VNA stimulus).

CHAPTER 4

Results

In this chapter I present a summary of the experimental results of this thesis. Sections 4.1-4.6 outlines and introduce the investigations presented in the appended papers while details and figures are contained in the corresponding papers. Section 4.7 is a self-contained text on the evaluation of a VIPA spectrometer for spinwave Brillouin spectroscopy performed in our laboratories. No paper is appended for this section, and hence all details are included.

4.1 Frequency comb Brillouin microscopy (Paper I)

In Paper I, the frequency-comb Brillouin microscope (FC-BLS) which was described in detail in chapter 3 is presented. The principle of operation of this technique has been discussed in Sec. 2.10 and 2.11 and it is also presented here together with the characterization of the instrument.

In the past decades pulsed laser sources, and more recently novel frequency combs, have been extensively used to improve Raman techniques and other types of optical spectroscopical methods. The implementation of ultrafast laser sources is a particularly difficult task in BLS. The extremely small frequency shift, the weak scattering amplitude and long integration times required in BLS make this technique incompatible with the characteristics of ultrafast excitation. There has been a tremendous increase of interest in ultrafast dynamics of laser driven magnons and acoustic phonons, and a variety of pump-probe methods have been developed to study such phenomena in the time-domain. However, there have been no reports to date that use BLS to study

such phenomena directly in the frequency-domain. The main reason for this is the low duty-cycle of laser sources used in most ultrafast experiments.

Paper I contains a proposal of a unique technique which combines the high sensitivity and resolution of BLS with ultrafast laser pumping. The key here is the very high repetition rate of the laser (1 GHz) employed. With such high duty cycles, observations of ultrafast dynamics using BLS are presented for first time. Furthermore, the highly structured features of the frequency comb allow a certain degree of coherent control of the excitation. Rather than observing a continuous broadening of the probe laser, only modes at harmonics of the repetition rate of the frequency comb are present in the Brillouin spectrum. The above is particularly essential in implementing a broadband excitation in BLS while maintaining mode-selectivity.

The characterization of the microscope system has been discussed in detail in 3.2 and it is presented in Paper I. The microscope lateral spatial resolution was characterized by measuring the probe and pump beam waist using a knife-edge method. Waist values of $\sim$ 313 nm and $\sim$ 730 nm for the probe and pump beam were measured, respectively. The pump beam pulse duration after the microscope objective and the scanning optics was estimated to be 120 fs. The thermal drift in the position of the femtosecond pump after the microscope was calculated from the specifications of the manufacturer of the mirror galvanometers to be 53 nm/°C with an accuracy of 80 nm. In practice, the accuracy of the scanning stage was much better than the estimated value. The main factor introducing errors was the accumulative drift of the mirror galvanometers in very long term measurements (over 12 hours).

As in stimulated Raman techniques, FC-BLS exhibits a non-linear scattering enhancement due to the action of the ultrafast laser source. The BLS from acoustic phonons follows a quadratic dependence against the pump power (see Paper I - Fig. 4b). This feature indicates a coherent and stimulated process. Furthermore, since the excitation is in the impulsive limit, it is possible to excite quasi-particles which propagate away from the pump spot.

Examples of two application which exploit the above features are demonstrated in

Paper I (see Paper I - Fig. 5). In a sapphire substrate coated with a 100 nm nickel film transducer, ultrafast periodic heating of the film by the laser action launches a phononic frequency comb which is the imaged with the BLS probe. The resolution and speed capabilities of the system are illustrated by producing a 20×20 μm (81×81 pixels) map of the acoustic mode at 6 GHz with 250 nm scanning step. This measurement was performed in $\sim$ 2 hours, which is exceptionally fast compared with typical 2D recording times in BLS.

Secondly, an application to generate a point source of ultrafast generated spinwaves is demonstrated. Such spinwaves are produced by periodic ultrafast demagnetization of a 20 nm permalloy (Py) film. The periodic modulation excites a high-amplitude and quasi-monochromatic surface mode at 8 GHz which exhibits ballistic propagation. This map was obtained in only 45 minutes for a matrix size of 51×21 pixels (total area of 5×2 μm).

The fast acquisition speed attainable using ultrafast pumping was critical for the subsequent studies presented in Papers II-V. Without the enhanced speed provided by the frequency comb, such studies involving 2D mapping would not be possible.

4.2 Thermal excitation of mode-selected propagating spinwaves (Paper II)

Most devices used in spintronics research are based on an 80/20 Ni/Fe magnetic alloy named Permalloy (Py). This alloy possesses an exceptionally high magnetic permeability, low coercivity and nearly zero magnetostriction. This material is extensively used in laminated magnetic cores and magnetic recording head sensors. Due to its outstanding magnetic properties and potential compatibility with silicon technologies, Py is a core material for constructing magnetic-active nanodevices [106].

Paper II contains an study in magnetodynamics driven by GHz pulsed pumping in the simplest case of thin Py films capped with a 2 nm Pt capping layer. The sample films were tested at different thicknesses and different capping materials which were typically used in the fabrication of SHNOs. No influence of the capping (2 nm thickness) in the

Py film response was found. The effect of the pumping is to excite the FRM and the spinwave band harmonically at multiples of 1 GHz. This effect occurs regardless of the film thickness (from 5 and up to at least 100 nm thickness). For this study a 20 nm film was chosen as a representative sample.

Due to the finite numerical aperture of the microscope objective (N.A.$= 0.75$ or a maximum cone angle of $49°$) the maximum detectable $k-$value is limited to 17.8 μrad/μm or a minimum wavelength of 350 nm. In between this range up to three modes in the spinwave band were observed to be excited by the laser. The samples could sustain a maximum pumping power of 35 mW before non-reversible changes in the magnetic anysotropy of the film material was observed. At this large pumping power the scattering enhancement of the FMR was up to three orders of magnitude larger than the thermal BLS. Tuning of the magnetic field strength from 0 to 1 Tesla shifts the spinwave band up to higher energies. The scattering enhancement was observed up to the 10$^{\text{th}}$ harmonic of the laser (see Paper II - Fig. 2).

Curiously, the spinwave amplitude vs. the pump laser intensity differs slightly, but noticeably, from a quadratic behavior (see Paper II - Fig. 3). In contrast, to single pulse experiments, in FC-BLS the sample is irradiated continuously with several mW of laser power. It is then reasonable to account for the rising in temperature due to laser heating with a Bloch law dependency in the spinwave BLS intensity as

$$I_{BLS} = A(t_r^{3/2} - (t_r^{3/2} + F)^{3/2})^2, \tag{4.1}$$

where F is the laser fluence, and A and t_r are coefficients which depend on the magnetization at absolute zero, the Curie and room temperatures, and the heating efficiency of the laser. Equation 4.1 was found to fit well with the experimental data.

Raster scanning of the femtosecond laser revealed the spinwave emission characteristics (see Paper II - Fig. 4). The propagation appear orthogonal to the in-plane component of the external bias magnetic field. This behavior agrees with a Damon-Eshbach spinwave mode also termed as a surface wave [107]. To corroborate that this

was the case, the in-plane component of the bias field was rotated by 30°, which made the spinwave propagation to rotate by the same amount. The decay length was found to be 1.85 μm, independent of the pump power. The experimental data was then compared with micromagnetic simulations of the periodic demagnetization field giving a good agreement (see Paper II - Fig. 5). In both, the simulations and the experimental data, the mode at 9 GHz shows a peculiar tendency to split up into four arms forming an X-shaped propagation profile.

4.3 Controllable spinwave caustics (Paper III)

Paper III contains investigations on X-shaped propagating spinwaves. Such intriguing propagation is the result of a caustic formation also termed as a self-focusing effect. It happens in materials with a certain type of anisotropy, in this case magnetic, and arises because the wave group and phase velocities are non-collinear in the media. As a consequence, phase interference allows the spinwave energy to be concentrated non-diffractively in specific directions. Fine tuning of the external magnetic field enables the creation of spinwave caustic beams with a controllable propagation angle in the range $\pm 12^{\circ}$, with respect to the direction orthogonal to the in-plane component of the magnetic bias (see Paper III - Fig. 3). Paper III also contains a theoretical calculation of the isofrequency surfaces $f_0(\mathbf{k})$ for the spinwave mode at 8 GHz. By definition the isofrequency curves are orthogonal to the group velocity vector $\mathbf{v}_{gf}$. Therefore, in the flat regions of $f_0(\mathbf{k})$ all wavevectors have the same direction of $\mathbf{v}_{gr}$. The condition to find a caustic beam propagation direction is then given by the zeroing of the second derivate of $f_0(\mathbf{k})$. For a certain spinwave frequency, the $k-$vector decreases as the bias field increases. As $k \longrightarrow 0$ the slope of the isofrequency curve approaches zero everywhere and the propagation appears primarily along the direction orthogonal to the in-plane bias field.

It is interesting to note that although the formation of caustic spinwave beams with a controllable emission angle have been previously demonstrated using patterned spinwave waveguides on top of thin films [108, 109], this is the first experimental demon-

stration of purely optically driven caustic beams. In early ultrafast magneto-optical experiments, Au *et al.* [110] concluded from simulations that a tight focused femtosecond laser actually produces a caustic spinwave. However, they could not observe this features experimentally. While Au *et al.* performed a single pulse experiment, FC-BLS has the advantage of producing a high-amplitude sustained spinwave, which enabled the observation such sensitive features for the first time.

4.4 Excitation of quantized perpendicular standing spinwaves (Paper IV)

Quantized perpendicular standing spinwaves (PSSWs) are modes which have their wave vector perpendicular to the film surface. They can be understood as standing waves in a resonant cavity consisting of the two surfaces of the film, where the wave vector k is quantized as $k = \pi n/d$. Here n is an integer number and d is the thickness of the film. Paper IV contains an study on the excitation of PSSW modes in Py films and the efficiency of the frequency comb excitation as a function of the film thicknesses in a range of 20-100 nm.

The efficiency characterization was performed by varying the film thickness and comparing the FC-BLS amplitude under identical conditions. A constant external field of 6000 Oe and the spinwave mode at 8 GHz, which appears for all film thickness just above the FMR, were chosen as fixed parameters. The BLS scattering as a function of the laser fluence follows Eq. 4.1 for all thicknesses (see Paper IV - Fig. 2). In Eq. 4.1 the parameter A can be interpreted as a measurement of the demagnetization. The excitation efficiency was then evaluated by studying A as a function of d. Assuming the demagnetization is proportional to the spinwave bath temperature, and the laser beam to be uniformly absorbed by the film, a relation $A \propto 1/d$ is expected. For film thicknesses < 30 nm the temperature rise due to optical absorption is no longer constant and instead depends on d. This effect was accounted for by weighing the experimental data with the thickness dependent optical absorption found by a simulation. The efficiency was the found to follow a $1/d$ dependence with a slight deviation for the thicker film (100

nm) (see Paper IV - Fig. 3). In this case, the assumption of uniform heating may no longer be valid considering the short penetration depth of the light (~ 10 nm).

The excitation laser has a very high excitation bandwidth. Therefore, in principle any mode within the bandwidth of the laser, or which period is considerable shorter than the laser pulse duration (120 fs), can be excited. The excitation frequency is however limited by the spinwave lifetime and the excitation efficiency per pulse. Paper IV exhibits the excitation of PSSW modes up to the 18^{th} harmonic, corresponding to the first three quantized modes (see Paper IV - Fig. 4). The excitation efficiency decreases as the spinwave energy increases. Finally, the enhancement of the 1^{st} order PSSW mode was observed higher than the FMR and other spinwave modes.

4.5 Generation of phononic caustic combs (Paper V)

In supported metallic thin films under femtosecond laser irradiation, surface and bulk acoustic waves are excited thermoelastically and launched into the substrate. Here, the film acts as a heat transducer which converts the laser energy into mechanical energy. In crystalline substrates, intriguing ballistic propagation patterns of the acoustic energy flux appear due to the lattice anisotropy [111]. Imaging such phenomena with millimetric spatial resolution has been performed at temperatures < 10 K using time-of-flight techniques [112], and at room temperature using scanning ultrasonic microscopy [113]. Recently, phonon imaging with micron resolution was achieved using microwave impedance microscopy [114], based on a cantilever probe, and ultrafast pump-probe spectroscopy, which uses a laser probe. This last method enables observation of ultrafast acoustic phenomena in the time-domain [111].

There has not been any reported observation of ultrafast generated acoustic dynamics, neither its propagation visualization, in the frequency domain. The first BLS imaging of laser driven phononic caustics at room temperature with sub-micron resolution using the advantages of FC-BLS are presented in Paper V. The experiment was performed in sapphire and quartz as test samples due to its contrasting properties. While sapphire is a highly isotropic material [115], quartz possesses a highly anisotropic crys-

tallographic structure. Acoustic waves in sapphire propagate approximately twice fast than in quartz [115, 116].

The action of the frequency comb on the metallized face of the crystals is to create point source from which a phononic frequency comb emanates. The phononic comb inherits the 1 GHz spectral structure of the laser. Propagation of phonons up to the 7$^{\text{th}}$ harmonic and several microns away from the pumping spot was observed. Beautiful acoustic flux patterns which reassemble the crystallographic plane structure of the crystals are seen in the BLS mapping (see Paper V - Fig. 2). In C-cut sapphire and Z-cut quartz, which posses an hexagonal 2-dimensional lattice, hex-geometrical propagation patterns and the formation of 6 caustics beams are observed. Surprisingly, in C-cut sapphire the propagation geometrical shapes rotate by 60° after the 4$^{\text{th}}$ harmonic and only two parallel caustics began to form as the frequency increases. The BLS maps show an interesting interference effect which redistributes the scattering in periodic rings around the source. The rings formation can be explained as a consequence of the interference of two co-propagating acoustic modes with the same temporal frequency but different velocities. Therefore, the ring wavefronts can be related to the isofrequency contours of the crystals. Furthermore, in quartz the density of fringes per micron at a fixed frequency increases with respect to sapphire, consistent with a slower acoustic velocity of the first material.

The BLS intensity as a function of the distance to the phonon source x was modeled as

$$I(x) = \frac{1}{x}[A_1^2 + A_2^2 + 2A_1A_2\text{cos}(\Delta kx + \phi)] + bg, \tag{4.2}$$

where A_1 and A_2 are the amplitude of the two waves, $\Delta k = k_2 - k_1$ their wave vector difference, ϕ is a spatial offset, and bg a background term arising from dark counts and the Rayleigh scattering wing. The $1/x$ decay accounts for the surface spreading from the source. Equation 4.2 provides a reasonable fit to the experimental data and a simple interpretation. The wave vector difference Δk dependence on the temporal frequency yields an acoustic-like dispersion. Without further assumptions, the available information provided by the experiment is still insufficient to recognize the independent

wave vectors of the interfering waves.

Further investigations on R-cut sapphire and X-cut quartz are also presented in Paper V. These crystallographic planes exhibit a pseudo-rectangular lattice structure, which is observed in the BLS propagation maps (see Paper V - Fig. 3). In R-cut sapphire 4 caustic beams are observed. Similar wave vector values to which where observed for C-sapphire were found, consistent with the known isotropic characteristics of sapphire. On the other hand, the X-cut quartz surface posses a highly anisotropic thermal conductivity along its principal axes [117]. This characteristic is revealed in the pronounced asymmetry of the BLS maps. Here two parallel caustic beams at the 2^{th} and 3^{th} harmonic and the gradual appearance of a second set of caustics orthogonal to the first ones at the 4^{th} and 5^{th} harmonics were observed.

To conclude, Paper V contains a beautiful application of this technique to reproduce a phononic version of the Young's experiment (see paper V - Fig. 4). The two point-source experiment was produced by splitting pump beam into two sources using a Michelson interferometer. This proof-of-principle highlights the applications of FC-BLS in phonon "optics" and related phenomena in media, without the requirement for in-built source generators. The ability to create a point-source of highly coherent and monochromatic quasi-particles by optical means can open the door and spur more studies of this type.

4.6 FR-MOKE Brillouin microscope (Paper VI)

In the pursuit of the development of a commercial optical FMR Brillouin spectrometer, Paper VI contains a discussion on an alternative method capable of overcoming the limitations presented by the TFPI system. Such limitations have been already discussed in this thesis and relate to the cost, size, operation expertise, room conditions and acquisition time requirements of the TFPI. In Paper VI, a novel optical technique based on the frequency-resolved magneto-optical Kerr-effect (FR-MOKE) is proposed and examined. Such a technique promises a path towards a commercial FMR spectrometer platform able to perform contact-free spatially-resolved measurements in a compact

and user-friendly design which allows miniaturization. The FR-MOKE method is very attractive since it completely removes the optical analysis unit (TFPI) and replaces it by only a high speed photodiode and a VNA unit. This tremendous simplification eliminates all the limitations imposed by having a sensitive optical bench in the system. Direct applications of this technique are envisioned for future SHNO-based computing schemes such as micro-Ising machines and neuromorphic devices [105].

SHNO are devices made by a NiFe/Pt bilayer nano-constrictions which are subject to an electrical DC current. Electrons traveling on the Pt layer are subject to the spin-Hall effect [118] and split into a spin-polarized current which flows into the NiFe layer inducing precession of the magnetic vector. Such oscillations modulates the nano-constriction resistance producing an RF field. In Paper VI, FR-MOKE detection is demonstrated. Identical capabilities and additional advantages in the characterization of SHNO devices compared to conventional electrical characterization are shown. While in an electrical measurement the power spectral density (PSD) of the SHNO is averaged over the entire device, FR-MOKE provides spatially-resolved PSD measurements with a diffraction-limited resolution. The influence of the laser and RF stimulus on the SHNO spectrum is also investigated (see Paper VI - Fig. 3). All the quantities of interest, such as the center frequency, linewidth, and peak intensity showed relationships to the RF and laser stimuli which can be linearized by a $\log_{10}$ transformation (see Paper VI - Fig. 4). Broadening and spectral shift were found to be < 100 MHz, and are only noticeable by means of the high frequency resolution of the VNA. Such small changes can be neglected in most practical applications. As a comparison, the maximum frequency resolution of a TFPI is ~ 100 MHz. A remarkable S/N ~ 25 on single SHNO characterization is demonstrated over a measurement bandwidth of 10 Hz and an average factor of 10.

Paper VI also contains an application using the second harmonic pumped FR-MOKE setup presented in Sec. 3.3.3. Here, spatially and phase resolved measurements of mutually synchronized SHNOs are shown (see Paper VI - Fig. 5). The results correspond to a system of two 120 nm width SHNOs separated by 300 nm, which was locked to

four different binary phase states with respect to each other. With a measurement bandwidth of 10 Hz (acquisition time per pixel of 102.3 ms), the magnitude maps show a S/N as large as 60. The phase maps show an S/N $\sim$ 18. It is shown that the phase contrast can be further enhanced by a factor of two by instead looking at the imaginary component of the spectrum. It is interesting to note that although the dimensions of the SHNO array are below the diffraction limit of the microscope, FR-MOKE provides sufficient contrast to identify all SHNOs states independently. The acquisition speed using FR-MOKE detection enormously surpasses the capabilities of a TFPI measurement. With the latter, 2D SHNO phase mappings are unpractical due to the extremely long acquisition time per pixel.

4.7 Investigations on a VIPA-based Brillouin miscroscope

The development of the optical virtual-image phase array (VIPA) represents an important milestone in the history of Brillouin spectroscopy. The first demonstration of a VIPA-based Brillouin spectrometer was in 2008 by Scarcelli *et al.* [102]. The authors presented an unprecedented and elegant solution that circumvented most of the complexity of the TFPI. In contrast to a TFPI, Scarcelli's solution is based only on a few optical elements with no moving parts, which reduces the instrument's cost drastically, as it does not require a vibration isolation platform, nor special room conditions. Additionally, the expertise required for the operation and maintenance of a VIPA spectrometer is far simpler than what is required for a TFPI. These advantages benefited the wide-spreading of applications of Brillouin spectroscopy in emerging research fields such as elastography [119, 120], mechanobiology [121–123] and biomedical sciences [124]. In spite of such advances, applications of the VIPA-technology for spinwave imaging has not been reported so far.

This section presents an evaluation of a VIPA spectrometer for its use in FMR microscopy. Although VIPA-technology has been very successful in the field of biophysics and could yield several benefits to the field of magnetic research, its implementation in the latter field is not trivial. The Brillouin scattering from magnetic structures

is far weaker than in biomaterials. In addition, in opaque metallic compounds, the BLS laser can only penetrates a few nanometers into the material, with extremely weak scattering cross-sections.

The VIPA experimental setup is presented in detail in Sec. 3.3.1 and it is shown in Fig. 4.1 for completeness. A Py film of 20 nm thickness was chosen for analysis as this compound is a central material in the construction of magnetic nano-devices. Moreover, the FC-BLS approach has been implemented in order to provide an additional enhancement factor in the scattering amplitude of the sample.

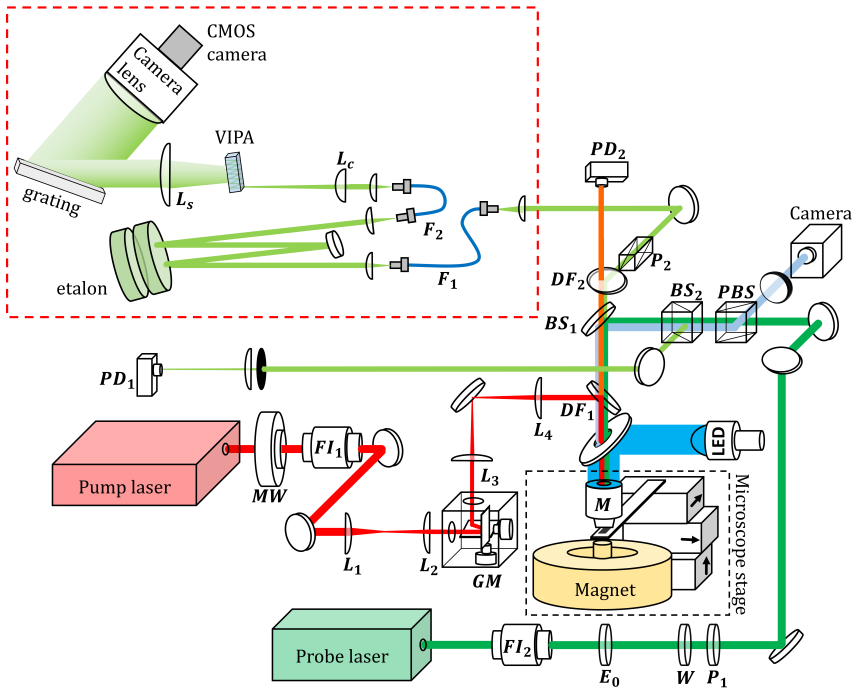

Fig. 4.1 Experimental setup. The red dotted rectangle shows the VIPA spectrometer arrangement. F_1 is the coupling fiber to the spectrometer, F_2 is a fiber link which connects the suppression filter with the dispersive block. The elements L_c and L_s correspond to a cylindrical and an spherical lens, respectively. All other lenses shown in the VIPA setup are aspherical collimation lenses. The rest of the elements in the schematic follow the nomenclature from Fig. 3.1.

Let us first assess the spectral contrast of the VIPA spectrometer and compare this with a typical measurement's contrast requirements. The Rayleigh/Brillouin scattering

ratio for Py estimated from measurements performed with the TFPI is $\sim$ 120 dB. For the VIPA, the manufacturer specifies a contrast of 60 dB at 6 GHz. The Brillouin backwards scattering from magnons is rotated by $90°$, hence an additional suppression of the elastic peak by approximately 40 dB can be achievable by a Glan-Thomson polarizer. Aditionally, the VIPA unit possesses a double-pass etalon filter that provides an extra suppression of 20-30 dB. Therefore, the VIPA, together with the polarizer and etalon filter, achieves an estimated contrast of < 120 dB, which is the minimum contrast required to discriminate the Brillouin scattering of Py. Note that the contrast of TFPI is 140-160 dB without the additional 40 dB suppression provided by the Glan-Thomson polarizer.

Figure 4.2 shows the thermal spectrum of Py acquired with (a) the TFPI and (b) the VIPA spectrometer. The sample was subject to a 7200 Oe magnetic field. At this field value the FMR resonance is expected to appear at approximately 8 GHz. The integration time was set to 189 ms per channel, and a total recording time of 85 seconds for the TFPI and 60 seconds for the VIPA spectrometer. The exceptional contrast of the TFPI allows the discrimination of the BLS features, virtually-free from Rayleigh scattered light. Conversely, the VIPA spectrum is largely contaminated by the elastic peak which extends over several GHz. In the latter case, no Brillouin spectral features could be clearly recognized. Moreover, in the VIPA spectrum the elastic peak broadens and saturates the detector as the integration time is set to larger values. Saturation can not be avoided by background subtraction, but it can be prevented by splitting the integration is shorter exposures. This solution, however, did to give better results, presumably because the read-out noise of the detector exceeded the Brillouin signal in this case.

Figure 4.3 shows the FC-BLS enhanced spectrum of Py subject to a pumping power of 20 mW. The measurement conditions are identical as for Fig. 4.2. The measurement performed with the TFPI shows an enhancement factor at 8 GHz of ~ 20 dB. This additional contrast permits the observation of the Stokes and anti-Stokes peaks in the VIPA spectrum. It is clear from Fig. 4.2b that the Rayleigh tail covers the spectral region of interest. The spectral feature at 9 GHz, which is resolved by the TFPI, is not resolved in

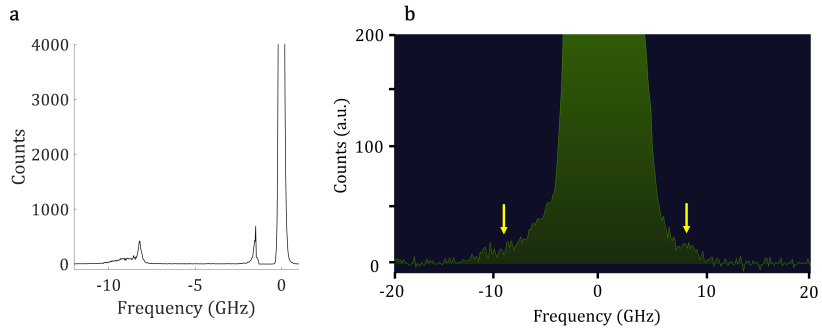

Fig. 4.2 Thermal Brillouin measurement comparison. **a**. TFPI measurement. **b**. VIPA measurement. Yellow arrows mark the positions where the FMR peak is expected.

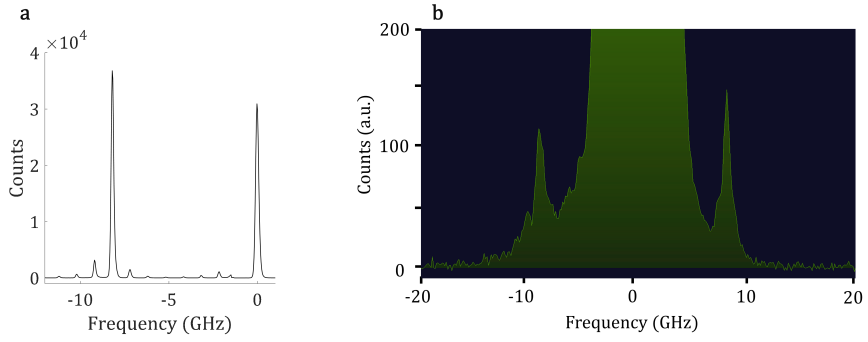

Fig. 4.3 FC-BLC measurement comparison **a**. TFPI measurement. **b**. VIPA measurement.

the VIPA spectrum. Figure 4.4 shows the 2D raw acquisition of 4.2b. Here, the bright feature at the center corresponds to the Rayleigh light. Blooming of the sensor in the read-out line (vertical direction) is observed. The Brillouin peaks can be identified in the image and are encircled in yellow. The red line represents the direction along which the Brillouin spectrum is extracted. Besides the 20 dB amplification factor, the spectrum obtained with the VIPA exhibits poor contrast. Hence, it can be concluded that at this stage the VIPA unit does not fulfill the sensitivity and spectral contrast requirements for spinwave imaging.

The instrument contrast can be further increased by suppressing the elastic peak by employing additional etalon filters or gas absorption cells. By employing the latter

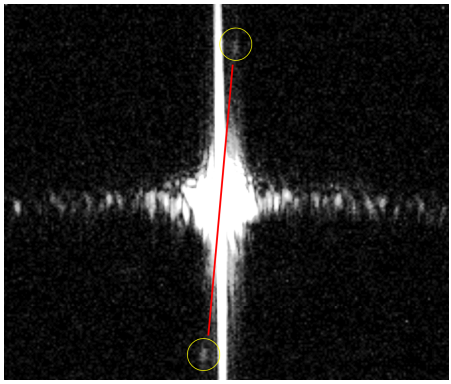

Fig. 4.4 2D raw spectral data. The Brillouin peaks are encircled in yellow. The red line represents the direction along which the 1D Brillouin spectrum is extracted.

mechanism, a suppression factor of 50 dB has been reported [125]. The poor sensitivity of the spectrometer is entirely related to the camera sensor (CMOS technology, Pixelink PL-D series), which could be improved, for instance by implementing instead a back-illuminated CCD sensor. Such detectors offer a large sensitivity with near 98% quantum efficiency, and a large well-capacity that may prevent saturation and excessive blooming at the Rayleigh peak. Such improvements are out of the scope of this work, but are presented, together with this evaluation, as part of a comprehensive roadmap to enable VIPA-based microscopy of spinwaves in the future.

To conclude, a recent study published in 2020 [126] presented a comparison between a TFPI and a commercial VIPA spectrometer (also from LightMachinery). The study shows a similar performance in both systems. However, the authors mention the employment of a VIPA unit with a smaller FSR (30 GHz), two double-pass etalon filters, and reported an spectral resolution of 0.1 GHz. With such improvements, the authors reported a maximum contrast of 120 dB. This gives their instrument 30 dB larger contrast, and 10 times higher spectral resolution than in the unit evaluated in this work. This work suggests that the VIPA technology will be improved and become suitable for more sensitive applications in a future, as for instance, in spintronics research.

CHAPTER 5

Outlook and conclusion

When my colleagues and I started this project in 2016, we did not know what we would discover. We merely started with the question of what would happen if we pumped a magnetic oscillator in resonance using a very high repetition rate femtosecond laser. To accomplish this apparently simple task, we built a completely new facility and designed new experimental protocols. By that time, GHz repetition rate lasers were just introduced to the market and this line of research began to become more popular. There were only few references in the literature, and none of them using Brillouin light scattering.

Today, I believe this work has served to establish a unique technique, which has been termed as frequency-comb Brillouin microscopy. This technique shows for the first time ultrafast dynamics captured with BLS, which is a time-average technique in the frequency-domain. This is in contrast to the extensive literature in the topic, which is based almost entirely on time-domain techniques such as time-resolved MOKE spectroscopy. The high sensitivity and large scattering cross-section provided by this technique permits the microscopic imaging of laser driven spinwave and phonon propagation. Interesting phenomena, such as the generation of caustic combs, were discovered. The studies performed here on thin films will serve as the groundwork for future research on pulsed laser driven SHNOs and other spintronics devices.

Four years later, by the time I completed this thesis, the University of Gothenburg had two running BLS laboratories (BLSlab1 and BLSlab2), both fully automatized and

equipped with an ultrafast laser scanning stage. Both laboratories were built together by myself and my co-workers Ahmad Awad and Shreyas Muralidhar in a combined effort. In this efforts, I was the main person responsible for designing and building the optical assemblies, and writing the code of the user interfaces that control the optical systems. The second BLS laboratory (BLSlab2) was finished in 2019 with several improvements over the first BLS laboratory (BLSlab1) which was used for most of the work presented in Papers I-V. The spatial resolution and the robustness of alignment of the BLSlab2 laboratory were enormously improved by implementing a high power single-mode optical coupling to guide the probe beam from the optical table to the BLS microscope top. The fiber works as an spatial filter which produces a clean gaussian beam profile at the output. It also helps to simplify the routinely alignment of the microscope to only one optical element (the fiber). After the optical fiber, the beamplitter cubes were replaced instead by orthogonal beamplitter plates which compensate each other from optical aberrations. These simple changes in the probe beam path reduced the measured beam waist after the microscope from 320 to 190 nm increasing the spatial resolution of the BLSlab2 system by 40%.

The ambition to pursue a BLS system which could be merchantable for spintronics research lead me to an extensive investigation on alternatives to dispense with the TFPI analyser. I then introduced two alternative approaches, one based on optical detection using a VIPA spectrometer and a second option based on electrical detection exploiting the MOKE effect.

The alternative, based on a VIPA spectrometer did not prove to achieve the minimum contrast required in a typical FMR measurement. In principle, additional suppression filters could be added to the VIPA in order to reach a similar performance of the TFPI. However, by adding filtering stages the VIPA station could become as expensive and complex as a TFPI unit. Therefore, I stopped further developments in this direction. Nevertheless, I believe further improvements in this technology will soon be made by others, making Brillouin spectroscopy a more accessible tool for research.

On the other hand, electrical detection using FR-MOKE proved to be an elegant and

promising approach. Using this method, I demonstrate high-resolution 2-dimensional phase maps of SHNO devices within one hour of measurement time. This is remarkable in comparison with previous phase-resolved BLS measurements of the same devices in which only 1-dimensional phase profiles were possible due to the excessive acquisition time required (tens of hours) in order to record 2-dimensional maps. Today, BLSlab1 at our university is equipped with an automatized FR-MOKE microscope system.

I believe that progress in electronics will soon allow a complete migration from bulky Brillouin optical spectrometers to electrical detection. Efforts in this direction have been already accomplished. A. Bilenca has recently demonstrated a high-speed stimulated Brillouin microscope which uses lock-in detection and a frequency-tunable pump laser [127]. Here, the optical analyser has been made unnecessary in the setup. However, this system still requires a complicated optical assembly for the excitation laser and to reference the Brillouin frequency. I believe a stimulated Brillouin microscope can be realized with only few optical elements by using the same detection principle as presented in Paper VI. The pump and the Stokes(anti-Stokes) laser beams can be produced from a single frequency laser using a phase modulator (PM) driven at the Brillouin resonance. The PM frequency input can be fed by the VNA and therefore automatically referenced. The detection is done by a second laser (probe) using exactly the same configuration shown in Paper VI. Since the probe laser can be an arbitrary wavelength, the pump beam can be easily suppressed from detection by a commercial spectral filter. Lately, our group procured such a phase modulator and work on this route is in progress.

In conclusion, this thesis has established novel and unique Brillouin techniques, which have been demonstrated in studies of magnetic films, spinwave imaging, observation of phonon propagation in crystals, characterization of spintronics devices, and phase contrast imaging, to mention a few. The promise for these techniques in the short term lies in the field of spintronics. We are closer to a full optical control, readout, and laser synchronization of SHNO networks. Excitation of magnetoelastic modes (spinwave-phonon coupling) is also plausible and promises a fruitful scientific

outcome. In the long term, applications would be extended to emerging phononic technologies and quantum computing. Finally, the ideas presented here could benefit also other research fields where Brillouin tools are required, such as biological and medical physics.

REFERENCES

[1] Newton's prisms and his experiments on the spectrum. *Notes and Records of the Royal Society of London*, 36(1):13–36, 8 1981.

[2] Foil A. Miller. The History of Spectroscopy as Illustrated on Stamps:. *applied spectroscopy*, 37(3):219–225, 8 2016.

[3] Tillmon H. Pearson and Aaron J. Ihde. Chemistry and the spectrum before Bunsen and Kirchhoff. *Journal of Chemical Education*, pages 267–271, 1951.

[4] Ji-Xin Cheng and Xiaoliang Sunney Xie. *Coherent raman scattering microscopy*. CEC Press, Boca Raton, 1th edition, 2018.

[5] B. E. (Bertram Eugene) Warren. *X-ray diffraction*. Dover Publications, 1990.

[6] Roberto Bini, Lorenzo Ulivi, Jörg Kreutz, and Hans J. Jodl. High-pressure phases of solid nitrogen by Raman and infrared spectroscopy. *The Journal of Chemical Physics*, 112(19):8522, 5 2000.

[7] Carey PR. Raman crystallography and other biochemical applications of Raman microscopy. *Annual review of physical chemistry*, 57:527–554, 2006.

[8] F. López-Vergara, A. Galdámez, V. Manríquez, and Guillermo González. Crystal structure and Raman scattering characterization of Cu2Fe1-xCoxSnS4 chalcogenide compounds. *Solid State Sciences*, 49:54–60, 11 2015.

[9] D. J. (Derek J.) Gardiner, P. R. (Pierre R.) Graves, and H. J. (Heather J.) Bowley. *Practical Raman spectroscopy*. Springer-Verlag, 1989.

[10] Zhiwei Men, Wenhui Fang, Dongfei Li, Zhanlong Li, and Chenglin Sun. Raman spectra from Symmetric Hydrogen Bonds in Water by High-intensity Laser-induced Breakdown. *Scientific Reports 2014 4:1*, 4(1):1–5, 4 2014.

[11] Geo. Glockler. The Raman Effect. *Reviews of Modern Physics*, 15(2):111, 4 1943.

[12] W. E. Moerner and L. Kador. Optical detection and spectroscopy of single molecules in a solid. *Physical Review Letters*, 62(21):2535–2538, 5 1989.

[13] Taras Plakhotnik and Daniel Walser. Time Resolved Single Molecule Spectroscopy. *Physical Review Letters*, 80(18):4064, 5 1998.

[14] Adrián A. Budini. Open quantum system approach to single-molecule spectroscopy. *Physical Review A*, 79(4):043804, 4 2009.

[15] Halina. Abramczyk. *Introduction to laser spectroscopy*. Elsevier, 2005.

[16] N. Bloembergen. From nanosecond to femtosecond science. *Reviews of Modern Physics*, 71(2):S283, 3 1999.

[17] Ahmed H. Zewail. Femtochemistry: Atomic-Scale Dynamics of the Chemical Bond†. *Journal of Physical Chemistry A*, 104(24):5660–5694, 6 2000.

[18] Philip H Bucksbaum. The future of attosecond spectroscopy. *Science (New York, N.Y.)*, 317(5839):766–9, 8 2007.

[19] Ferenc Krausz and Misha Ivanov. Attosecond physics. *Reviews of Modern Physics*, 81(1):163, 2 2009.

[20] A. Laubereau and W. Kaiser. Vibrational dynamics of liquids and solids investigated by picosecond light pulses. *Reviews of Modern Physics*, 50(3):607, 7 1978.

[21] P. Mutti, C. E. Bottani, G. Ghislotti, M. Beghi, G. A. D. Briggs, and J. R. Sandercock. Surface Brillouin Scattering—Extending Surface Wave Measurements to 20 GHz. In *Advances in Acoustic Microscopy*, pages 249–300. Springer US, Boston, MA, 1995.

[22] Carlo E. Bottani and Daniele Fioretto. Brillouin scattering of phonons in complex materials. *Advances in Physics: X*, 3(1):1467281, 1 2018.

[23] G. B. Benedek and K. Fritsch. Brillouin Scattering in Cubic Crystals. *Physical Review*, 149(2):647, 9 1966.

[24] R. Vacher and L. Boyer. Brillouin Scattering: A Tool for the Measurement of Elastic and Photoelastic Constants. *Physical Review B*, 6(2):639, 7 1972.

[25] Thomas Sebastian, Katrin Schultheiss, BjÃ¶rn Obry, Burkard Hillebrands, and Helmut Schultheiss. Micro-focused Brillouin light scattering: imaging spin waves at the nanoscale. *Frontiers in Physics*, 3:35, 6 2015.

[26] J. R. Dutcher, J. F. Cochran, I. Jacob, and Jr W. F. Egelhoff. Brillouin light-scattering intensities for thin magnetic films with large perpendicular anisotropies. *Physical Review B*, 39(14):10430, 5 1989.

[27] Marco Madami, Gianluca Gubbiotti, Silvia Tacchi, and Giovanni Carlotti. Application of Microfocused Brillouin Light Scattering to the Study of Spin Waves in Low-Dimensional Magnetic Systems. *Solid State Physics*, 63:79–150, 1 2012.

[28] Ryan Freeman, Robert Lemasters, Tomi Kalejaiye, Feng Wang, Guanxiong Chen, Jinjun Ding, Mingzhong Wu, Vladislav E. Demidov, Sergej O. Demokritov, Hayk Harutyunyan, and Sergei Urazhdin. Brillouin light scattering of spin waves inaccessible with free-space light. *Physical Review Research*, 2(3):033427, 9 2020.

[29] S. O. Demokritov, B. Hillebrands, and A. N. Slavin. Brillouin light scattering studies of confined spin waves: linear and nonlinear confinement. *Physics Reports*, 348(6):441–489, 7 2001.

[30] Vladislav E. Demidov and Sergej O. Demokritov. Magnonic waveguides studied by microfocus brillouin light scattering. *IEEE Transactions on Magnetics*, 51(4), 4 2015.

[31] Michael Faraday; Thomas Martin. *Faraday's diary : being the various philosophical notes of experimental investigation*. HR Direct, Riverton, Utah, 2nd ed edition, 2008.

[32] VIII. A dynamical theory of the electromagnetic field. *Philosophical Transactions of the Royal Society of London*, 155:459–512, 1 1865.

[33] P. Weinberger. John Kerr and his effects found in 1877 and 1878. *Philosophical Magazine Letters*, 88(12):897–907, 12 2008.

[34] A K Zvezdin and V A Kotov. *Modern Magnetooptics and Magnetooptical Materials*. Taylor and Francis Group, New York, 1th edition, 1997.

[35] Riccardo Hertel. Theory of the inverse Faraday effect in metals. *Journal of Magnetism and Magnetic Materials*, 303(1):L1–L4, 8 2006.

[36] E. Beaurepaire, J.-C. Merle, A. Daunois, and J.-Y. Bigot. Ultrafast Spin Dynamics in Ferromagnetic Nickel. *Physical Review Letters*, 76(22):4250–4253, 5 1996.

[37] Amal El-Ghazaly, Jon Gorchon, Richard B. Wilson, Akshay Pattabi, and Jeffrey Bokor. Progress towards ultrafast spintronics applications. *Journal of Magnetism and Magnetic Materials*, 502:166478, 5 2020.

[38] Burkard Hillebrands and Jürgen Fassbender. Ultrafast magnetic switching. *Nature 2002 418:6897*, 418(6897):493–495, 8 2002.

[39] A. Stupakiewicz, K. Szerenos, D. Afanasiev, A. Kirilyuk, and A. V. Kimel. Ultrafast nonthermal photo-magnetic recording in a transparent medium. *Nature 2017 542:7639*, 542(7639):71–74, 1 2017.

[40] Karel Carva, Pavel Baláž, and Ilie Radu. Laser-Induced Ultrafast Magnetic Phenomena. *Handbook of Magnetic Materials*, 26:291–463, 1 2017.

[41] Kevin Bühlmann, Rafael Gort, Gerard Salvatella, Simon Däster, Andreas Fognini, Thomas Bähler, Christian Dornes, C. A. F. Vaz, Andreas Vaterlaus, and Yves Acremann. Ultrafast demagnetization in iron: Separating effects by their nonlinearity. *Structural Dynamics*, 5(4):044502, 7 2018.

[42] Wei Zhang, Wei He, Xiang-Qun Zhang, Zhao-Hua Cheng, Jiao Teng, and Manfred Fähnle. Unifying ultrafast demagnetization and intrinsic Gilbert damping in Co/Ni bilayers with electronic relaxation near the Fermi surface. *Physical Review B*, 96(22):220415, 12 2017.

[43] T. Ogasawara, K. Ohgushi, Y. Tomioka, K. S. Takahashi, H. Okamoto, M. Kawasaki, and Y. Tokura. General Features of Photoinduced Spin Dynamics in Ferromagnetic and Ferrimagnetic Compounds. *Physical Review Letters*, 94(8):087202, 3 2005.

[44] Jean-Yves Bigot, Mircea Vomir, and Eric Beaurepaire. Coherent ultrafast magnetism induced by femtosecond laser pulses. *Nature Physics*, 5(7):515–520, 7 2009.

[45] A. Kamimaki, S. Iihama, Y. Sasaki, Y. Ando, and S. Mizukami. Reciprocal excitation of propagating spin waves by a laser pulse and their reciprocal mapping in magnetic metal films. *Physical Review B*, 96(1):014438, 7 2017.

[46] S. Iihama, Y. Sasaki, A. Sugihara, A. Kamimaki, Y. Ando, and S. Mizukami. Quantification of a propagating spin-wave packet created by an ultrashort laser pulse in a thin film of a magnetic metal. *Physical Review B*, 94(2):020401, 7 2016.

[47] Keoki A. Seu and Anne C. Reilly. Ultrafast laser excitation of spin waves and the permanent modification of the exchange bias interaction in IrMnCo. *Journal of Applied Physics*, 103(7):07C104, 4 2008.

[48] C. D. Stanciu, F. Hansteen, A. V. Kimel, A. Kirilyuk, A. Tsukamoto, A. Itoh, and Th. Rasing. All-Optical Magnetic Recording with Circularly Polarized Light. *Physical Review Letters*, 99(4):047601, 7 2007.

[49] Fredrik Hansteen, Alexey Kimel, Andrei Kirilyuk, and Theo Rasing. Femtosecond Photomagnetic Switching of Spins in Ferrimagnetic Garnet Films. *Physical Review Letters*, 95(4):047402, 7 2005.

[50] V. N. Kats, T. L. Linnik, A. S. Salasyuk, A. W. Rushforth, M. Wang, P. Wadley, A. V. Akimov, S. A. Cavill, V. Holy, A. M. Kalashnikova, and A. V. Scherbakov. Ultrafast changes of magnetic anisotropy driven by laser-generated coherent and noncoherent phonons in metallic films. *Physical Review B*, 93(21):214422, 6 2016.

[51] Andrei Kirilyuk, Alexey V. Kimel, and Theo Rasing. Ultrafast optical manipulation of magnetic order. *Reviews of Modern Physics*, 82(3):2731–2784, 9 2010.

[52] Vitalyi Gusev. Laser hypersonics in fundamental and applied research. *Acustica*, 82:S37–S45, 1996.

[53] H. -N. Lin, R. J. Stoner, H. J. Maris, and J. Tauc. Phonon attenuation and velocity measurements in transparent materials by picosecond acoustic interferometry. *Journal of Applied Physics*, 69(7):3816, 8 1998.

[54] J.-Y. Duquesne and B. Perrin. Ultrasonic attenuation in a quasicrystal studied by picosecond acoustics as a function of temperature and frequency. *Physical Review B*, 68(13):134205, 10 2003.

[55] C. Thomsen, H. T. Grahn, H. J. Maris, and J. Tauc. Surface generation and detection of phonons by picosecond light pulses. *Physical Review B*, 34(6):4129, 9 1986.

[56] Pascal Ruello and Vitalyi E. Gusev. Physical mechanisms of coherent acoustic phonons generation by ultrafast laser action. *Ultrasonics*, 56:21–35, 2 2015.

[57] T. Saito, O. Matsuda, and O. B. Wright. Picosecond acoustic phonon pulse generation in nickel and chromium. *Physical Review B*, 67(20):205421, 5 2003.

[58] O. B. Wright and V. E. Gusev. Ultrafast acoustic phonon generation in gold. *Physica B: Condensed Matter*, 219-220(1-4):770–772, 4 1996.

[59] O. B. Wright. Ultrafast nonequilibrium stress generation in gold and silver. *Physical Review B*, 49(14):9985, 4 1994.

[60] P. Babilotte, P. Ruello, D. Mounier, T. Pezeril, G. Vaudel, M. Edely, J-M. Breteau, V. Gusev, and K. Blary. Femtosecond laser generation and detection of high-frequency acoustic phonons in GaAs semiconductors. *Physical Review B*, 81(24):245207, 6 2010.

[61] E. S. K. Young, A. V. Akimov, R. P. Campion, A. J. Kent, and V. Gusev. Picosecond strain pulses generated by a supersonically expanding electron-hole plasma in GaAs. *Physical Review B*, 86(15):155207, 10 2012.

[62] Yong Xin Yan, Edward B. Gamble, and Keith A. Nelson. Impulsive stimulated scattering: General importance in femtosecond laser pulse interactions with matter, and spectroscopic applications. *The Journal of Chemical Physics*, 83(11):5391–5399, 1985.

[63] Hajime Tanaka, Tsuyoshi Sonehara, and Shinsaku Takagi. A New Phase-Coherent Light Scattering Method: First Observation of Complex Brillouin Spectra. *Physical Review Letters*, 79(5):881, 8 1997.

[64] Xiaohan Shen, Zonghuan Lu, Yukta P. Timalsina, Toh-Ming Lu, Morris Washington, and Masashi Yamaguchi. Coherent Phonon Transport Measurement and Controlled Acoustic Excitations Using Tunable Acoustic Phonon Source in GHz-sub THz Range with Variable Bandwidth. *Scientific Reports*, 8(1):7054, 12 2018.

[65] C. Klieber, E. Peronne, K. Katayama, J. Choi, M. Yamaguchi, T. Pezeril, and Keith A. Nelson. Narrow-band acoustic attenuation measurements in vitreous silica at frequencies between 20 and 400 GHz. *Applied Physics Letters*, 98(21):211908, 5 2011.

[66] O. Synnergren, T. N. Hansen, S. Canton, H. Enquist, P. Sondhauss, A. Srivastava, and J. Larsson. Coherent phonon control. *Applied Physics Letters*, 90(17):171929, 4 2007.

[67] Florian Hudert, Axel Bruchhausen, Daniel Issenmann, Olivier Schecker, Reimar Waitz, Artur Erbe, Elke Scheer, Thomas Dekorsy, Adnen Mlayah, and Jean-Roch Huntzinger. Confined longitudinal acoustic phonon modes in free-standing Si membranes coherently excited by femtosecond laser pulses. *Physical Review B*, 79(20):201307, 5 2009.

[68] A. Bruchhausen, R. Gebs, F. Hudert, D. Issenmann, G. Klatt, A. Bartels, O. Schecker, R. Waitz, A. Erbe, E. Scheer, J.-R. Huntzinger, A. Mlayah, and T. Dekorsy. Subharmonic Resonant Optical Excitation of Confined Acoustic Modes in a Free-Standing Semiconductor Membrane at GHz Frequencies with a High-Repetition-Rate Femtosecond Laser. *Physical Review Letters*, 106(7):077401, 2 2011.

[69] Osamu Matsuda, Shogo Kaneko, Oliver Wright, and Motonobu Tomoda. Time-resolved gigahertz acoustic wave imaging at arbitrary frequencies. *IEEE Transactions on Ultrasonics, Ferroelectrics, and Frequency Control*, 62(3):584–595, 3 2015.

[70] Robert W. Boyd. *Nonlinear optics*. Academic Press, 2008.

[71] A.S. Borovik-Romanov and N.M. Kreines. Brillouin-Mandelstam scattering from thermal and excited magnons. *Physics Reports*, 81(5):351–408, 1 1982.

[72] S. M. Lindsay, M. W. Anderson, and J. R. Sandercock. Construction and alignment of a high performance multipass vernier tandem Fabry-Perot interferometer. *Review of Scientific Instruments*, 52(10):1478–1486, 10 1981.

[73] F. Scarponi, S. Mattana, S. Corezzi, S. Caponi, L. Comez, P. Sassi, A. Morresi, M. Paolantoni, L. Urbanelli, C. Emiliani, L. Roscini, L. Corte, G. Cardinali, F. Palombo, J. R. Sandercock, and D. Fioretto. High-performance versatile setup for simultaneous Brillouin-Raman microspectroscopy. *Physical Review X*, 7(3):31015, 7 2017.

[74] M. Shirasaki. Large angular dispersion by a virtually imaged phased array and its application to a wavelength demultiplexer. *Optics Letters*, 21(5):366, 3 1996.

[75] Xinrong Hu, Qiang Sun, Jing Li, Chun Li, Ying Liu, and Jianzhong Zhang. Spectral dispersion modeling of virtually imaged phased array by using angular spectrum of plane waves. *Optics Express*, 23(1):1, 1 2015.

[76] Francesca Palombo and Daniele Fioretto. Brillouin Light Scattering: Applications in Biomedical Sciences, 7 2019.

[77] Seok Hyun Yun and Dimitri Chernyak. Brillouin microscopy: Assessing ocular tissue biomechanics. *Current Opinion in Ophthalmology*, 29(4):299–305, 7 2018.

[78] Christine Poon, Joshua Chou, Michael Cortie, and Irina Kabakova. Brillouin imaging for studies of micromechanics in biology and biomedicine: from current state-of-the-art to future clinical translation. *Journal of Physics: Photonics*, 3(1):012002, 12 2020.

[79] M. L. Schneider, J. M. Shaw, A. B. Kos, Th Gerrits, T. J. Silva, and R. D. McMichael. Spin dynamics and damping in nanomagnets measured directly by frequency-resolved magneto-optic Kerr effect. *Journal of Applied Physics*, 102(10):103909, 11 2007.

[80] Lukas Liensberger, Luis Flacke, David Rogerson, Matthias Althammer, Rudolf Gross, and Mathias Weiler. Spin-wave propagation in metallic co25fe75 films determined by microfocused frequency-resolved magneto-optic kerr effect. *IEEE Magnetics Letters*, 10, 2019.

[81] Yuxin Sun, Masumi Saka, Jing Li, and Jialing Yang. Ultrafast laser-induced thermoelastic behavior in metal films. *International Journal of Mechanical Sciences*, 52(9):1202–1207, 9 2010.

[82] T. Brudevoll, A. K. Storebo, O. Skaaring, C. N. Kirkemo, O. C. Norum, O. Olsen, and M. Breivik. Time-Resolved Laser Spectroscopy of Semiconductors - Physical Processes and Methods of Analysis. *Femtosecond-Scale Optics*, 11 2011.

[83] N. Del Fatti, P. Langot, R. Tommasi, and F. Vallée. Ultrafast hole–phonon interactions in GaAs. *Applied Physics Letters*, 71(1):75, 6 1998.

[84] P. Yu and M. Cardona. *Fundamentals of Semiconductors* . Springer, Verlag, Heidelberg, 1998.

[85] Andrew C. Tam. Applications of photoacoustic sensing techniques. *Reviews of Modern Physics*, 58(2):381, 4 1986.

[86] A. Scholl, L. Baumgarten, R. Jacquemin, and W. Eberhardt. Ultrafast spin dynamics of ferromagnetic thin films observed by fs spin-resolved two-photon photoemission. *Physical Review Letters*, 79(25):5146–5149, 1 1997.

[87] Zhanghui Chen, Jun Wei Luo, and Lin Wang Wang. Revealing angular momentum transfer channels and timescales in the ultrafast demagnetization process of ferromagnetic semiconductors. *Proceedings of the National Academy of Sciences of the United States of America*, 116(39):19258–19263, 9 2019.

[88] D. Steiauf and M. Fähnle. Elliott-Yafet mechanism and the discussion of femtosecond magnetization dynamics. *Physical Review B - Condensed Matter and Materials Physics*, 79(14):140401, 4 2009.

[89] V. Gusev, P. Picart, D. Mounier, and J. M. Breteau. On the possibility of ultrashort shear acoustic pulse excitation due to the laser-induced electrostrictive effect. *Optics Communications*, 204(1-6):229–236, 4 2002.

[90] Fredrik Hansteen, Alexey Kimel, Andrei Kirilyuk, and Theo Rasing. Nonthermal ultrafast optical control of the magnetization in garnet films. *Physical Review B*, 73(1):014421, 1 2006.

[91] A. I. Chernov, M. A. Kozhaev, I. V. Savochkin, D. V. Dodonov, P. M. Vetoshko, A. K. Zvezdin, and V. I. Belotelov. Optical excitation of spin waves in epitaxial iron garnet films: MSSW vs BVMSW. *Optics Letters*, 42(2):279, 1 2017.

[92] Yuhao Zou, Haiwei Wang, Yao Xiao, Zhihao Zeng, Lanlan Huang, Kai Wang, Sicong Wang, Xiangping Li, Changsheng Xie, Yuhao Zou, Haiwei Wang, Yao Xiao, Zhihao Zeng, Lanlan Huang, Kai Wang, Sicong Wang, Xiangping Li, and Changsheng Xie. Theoretical Investigation of Laser Induced Magnetization Reversal by Spin Orbit Coupling and Stimulated Raman Scattering. *Applied Sciences*, 9(1):102, 12 2018.

[93] Paul Brumer and Moshe Shapiro. Scenarios in Coherent Control. In *Coherent Control in Atoms, Molecules, and Semiconductors*, chapter 1, page 220. Springer Science+Business Media, 1999.

[94] R. A. Bartels, S. Backus, M. M. Murnane, and H. C. Kapteyn. Impulsive stimulated Raman scattering of molecular vibrations using nonlinear pulse shaping. *Chemical Physics Letters*, 374(3-4):326–333, 6 2003.

[95] A. M. Weiner, Gary P. Wiederrecht, Keith A. Nelson, and D. E. Leaird. Femtosecond multiple-pulse impulsive stimulated Raman scattering spectroscopy. *Journal of the Optical Society of America B*, 8(6):1264, 6 1991.

[96] Y. J. Yan and S. Mukamel. Pulse shaping and coherent Raman spectroscopy in condensed phases. *The Journal of Chemical Physics*, 94(2):997–1005, 1991.

[97] Andrew M. Weiner. Ultrafast Optics. In *Ultrafast Optics*, chapter 9, pages 499–505. John Wiley and Sons, Inc., Hoboken, NJ, USA, 6 2009.

[98] J. D. Choi, T. Feurer, M. Yamaguchi, B. Paxton, and K. A. Nelson. Generation of ultrahigh-frequency tunable acoustic waves. *Applied Physics Letters*, 87(8):081907, 8 2005.

[99] Richard A. McCracken, Jake M. Charsley, and Derryck T. Reid. A decade of astrocombs: recent advances in frequency combs for astronomy [Invited]. *Optics Express*, 25(13):15058, 6 2017.

[100] Gabriel G. Ycas, Franklyn Quinlan, Scott A. Diddams, Steve Osterman, Suvrath Mahadevan, Stephen Redman, Ryan Terrien, Lawrence Ramsey, Chad F. Bender, Brandon Botzer, and Steinn Sigurdsson. Demonstration of on-sky calibration of astronomical spectra using a 25 GHz near-IR laser frequency comb. *Optics Express*, 20(6):6631, 3 2012.

[101] J. Trägårdh, K. Macrae, C. Travis, R. Amor, G. Norris, S. H. Wilson, G. L. Oppo, and G. Mcconnell. A simple but precise method for quantitative measurement of the quality of the laser focus in a scanning optical microscope. *Journal of Microscopy*, 259(1):66–73, 7 2015.

[102] Giuliano Scarcelli and Seok Hyun Yun. Confocal Brillouin microscopy for three-dimensional mechanical imaging. *Nature Photonics*, 2(1):39–43, 1 2008.

[103] Anett Jannasch, Jan Rix, Roberta Galli, Claudia Dittfeld, Edmund Koch, Klaus Matschke, Gabriele Schackert, and Sems-Malte Tugtekin. Brillouin Spectroscopy as an Innovative Tool to Investigate Biomechanical Properties of Native Human Aortic Valve and Bioprostheses Tissue. *https://doi.org/10.1080/24748706.2021.1901535*, 5(sup1):29–29, 4 2021.

[104] Peng Shao, Amira M. Eltony, Theo G. Seiler, Behrouz Tavakol, Roberto Pineda, Tobias Koller, Theo Seiler, and Seok-Hyun Yun. Spatially-resolved Brillouin spectroscopy reveals biomechanical abnormalities in mild to advanced keratoconus in vivo. *Scientific Reports 2019 9:1*, 9(1):1–12, 5 2019.

[105] Mohammad Zahedinejad, Ahmad A. Awad, Shreyas Muralidhar, Roman Khymyn, Himanshu Fulara, Hamid Mazraati, Mykola Dvornik, and Johan Åkerman. Two-dimensional mutually synchronized spin Hall nano-oscillator arrays for neuromorphic computing. *Nature Nanotechnology*, 15(1):47–52, 1 2020.

[106] Gesche Nahrwold, Jan M. Scholtyssek, Sandra Motl-Ziegler, Ole Albrecht, Ulrich Merkt, and Guido Meier. Structural, magnetic, and transport properties of Permalloy for spintronic experiments. *Journal of Applied Physics*, 108(1):13907, 7 2010.

[107] Jonathan Trossman, Jinho Lim, Wonbae Bang, J. B. Ketterson, C. C. Tsai, and S. J. Lee. Effects of an adjacent metal surface on spin wave propagation. *AIP Advances*, 8(5):056024, 1 2018.

[108] T. Schneider, A. A. Serga, A. V. Chumak, C. W. Sandweg, S. Trudel, S. Wolff, M. P. Kostylev, V. S. Tiberkevich, A. N. Slavin, and B. Hillebrands. Nondiffractive subwavelength wave beams in a medium with externally controlled anisotropy. *Physical Review Letters*, 104(19):197203, 5 2010.

[109] Vladislav E. Demidov, Sergej O. Demokritov, Daniel Birt, Brian O'Gorman, Maxim Tsoi, and Xiaoqin Li. Radiation of spin waves from the open end of a microscopic magnetic-film waveguide. *Physical Review B - Condensed Matter and Materials Physics*, 80(1):014429, 8 2009.

[110] Y. Au, M. Dvornik, T. Davison, E. Ahmad, P. S. Keatley, A. Vansteenkiste, B. Van Waeyenberge, and V. V. Kruglyak. Direct excitation of propagating spin waves by focused ultrashort optical pulses. *Physical Review Letters*, 110(9):097201, 2 2013.

[111] Y. Sugawara, O. B. Wright, O. Matsuda, M. Takigahira, Y. Tanaka, S. Tamura, and V. E. Gusev. Watching Ripples on Crystals. *Physical Review Letters*, 88(18):185504, 4 2002.

[112] G. A. Northrop and J. P. Wolfe. Ballistic Phonon Imaging in Solids—A New Look at Phonon Focusing. *Physical Review Letters*, 43(19):1424, 11 1979.

[113] Matt R. Hauser, R. L. Weaver, and J. P. Wolfe. Internal diffraction of ultrasound in crystals: Phonon focusing at long wavelengths. *Physical Review Letters*, 68(17):2604, 4 1992.

[114] Thorsten Hesjedal and Gerd Behme. AFM observation of surface acoustic waves emitted from single symmetric SAW transducers. *IEEE Transactions on Ultrasonics, Ferroelectrics, and Frequency Control*, 48(3):641–642, 5 2001.

[115] G. I. Kanel, W. J. Nellis, A. S. Savinykh, S. V. Razorenov, and A. M. Rajendran. Response of seven crystallographic orientations of sapphire crystals to shock stresses of 16–86 GPa. *Journal of Applied Physics*, 106(4):043524, 8 2009.

[116] Jun-ichi Kushibiki, Masanori Ohtagawa, and Izumi Takanaga. Comparison of acoustic properties between natural and synthetic α-quartz crystals. *Journal of Applied Physics*, 94(1):295, 6 2003.

[117] Lei Tang and Chris Dames. Anisotropic thermal conductivity tensor measurements using beam-offset frequency domain thermoreflectance (BO-FDTR) for materials lacking in-plane symmetry. *International Journal of Heat and Mass Transfer*, 164:120600, 1 2021.

[118] J. E. Hirsch. Spin Hall Effect. *Physical Review Letters*, 83(9):1834, 8 1999.

[119] Kaiwen Zhang, Min Zhu, Evan Thomas, Sevan Hopyan, and Yu Sun. Existing and Potential Applications of Elastography for Measuring the Viscoelasticity of Biological Tissues In Vivo. *Frontiers in Physics*, 0:294, 6 2021.

[120] Achuth Nair, Giuliano Scarcelli, Jitao Zhang, Kirill V. Larin, Manmohan Singh, Salavat R. Aglyamov, Yogeshwari S. Ambekar, and Kirill V. Larin. Multimodal quantitative optical elastography of the crystalline lens with optical coherence elastography and Brillouin microscopy. *Biomedical Optics Express, Vol. 11, Issue 4, pp. 2041-2051*, 11(4):2041–2051, 4 2020.

[121] Giuseppe Antonacci and Sietse Braakman. Biomechanics of subcellular structures by non-invasive Brillouin microscopy. *Scientific Reports*, 6(1):37217, 12 2016.

[122] Giuliano Scarcelli. Brillouin microscopy for tissue and cell biomechanics. *Frontiers in Optics 2015 (2015), paper FM2F.2*, page FM2F.2, 10 2015.

[123] Robert Prevedel, Alba Diz-Muñoz, Giancarlo Ruocco, and Giuseppe Antonacci. Brillouin microscopy: an emerging tool for mechanobiology, 10 2019.

[124] Francesca Palombo and Daniele Fioretto. Brillouin Light Scattering: Applications in Biomedical Sciences, 7 2019.

[125] Andrew J. Traverso, Vladislav V. Yakovlev, and Zhaokai Meng. Background clean-up in Brillouin microspectroscopy of scattering medium. *Optics Express, Vol. 22, Issue 5, pp. 5410-5415*, 22(5):5410–5415, 3 2014.

[126] Antony Bazir, Guqi Yan, Jeremie Margueritat, and Thomas Dehoux. Evaluation of commercial virtually imaged phase array and Fabry-Pand#x00E9;rot based Brillouin spectrometers for applications to biology. *Biomedical Optics Express, Vol. 11, Issue 12, pp. 6933-6944*, 11(12):6933–6944, 12 2020.

[127] Itay Remer, Roni Shaashoua, Netta Shemesh, Anat Ben-Zvi, and Alberto Bilenca. High-sensitivity and high-specificity biomechanical imaging by stimulated Brillouin scattering microscopy. *Nature Methods 2020 17:9*, 17(9):913–916, 8 2020.